inorganics

MDPI

Article

Mixed-Valence Pentadecavanadate with Ca^{2+}-ATPase Inhibition Potential and Anti-Breast Cancer Activity

Bianca R. Brito [1,†], Heloísa de S. Camilo [1,†], Anderson F. da Cruz [2], Ronny R. Ribeiro [1], Eduardo L. de Sá [1], Carolina Camargo de Oliveira [2], Gil Fraqueza [3,4], Giseli Klassen [5], Manuel Aureliano [3,6,*] and Giovana G. Nunes [1,*]

1 Departamento de Química, Universidade Federal do Paraná, Curitiba 81531-980, Brazil; ronny.ribeiro@ufpr.br (R.R.R.)
2 Departamento de Biologia Celular, Universidade Federal do Paraná, Curitiba 81531-980, Brazil; andersonfraga@ufpr.br (A.F.d.C.); krokoli@ufpr.br (C.C.d.O.)
3 Centro de Ciências do Mar, Universidade do Algarve, 8000-139 Faro, Portugal; gfraque@ualg.pt
4 Instituto Superior de Engenharia, Universidade do Algarve, 8000-139 Faro, Portugal
5 Departamento de Patologia Básica, Universidade Federal do Paraná, Curitiba 82590-300, Brazil; giseli@ufpr.br
6 Faculdade de Ciências e Tecnologia, Universidade do Algarve, 8005-139 Faro, Portugal
* Correspondence: cmaalves@ualg.pt (M.A.); nunesgg@ufpr.br (G.G.N.)
† These authors contributed equally to this work.

Abstract

Polyoxovanadates are a subclass of polyoxometalates (POMs) known to interact with proteins and to present anticancer, antimicrobial, and antiviral activities. Herein, we aimed to pursue the study of the breast anticancer activity of a mixed-valence polyoxovanadate, $[Cl@V^{V}_{7}V^{IV}_{8}O_{36}]^{6-}$ (V_{15}) against MCF-7 and MDA-MB-231 cancer cell lines and to analyze its Ca^{2+}-ATPase inhibition potential. ^{51}V NMR and UV-Vis/NIR studies of V_{15} indicated its stability in HEPES and RPMI media. For the Ca^{2+}-ATPase activity, V_{15} showed an IC_{50} value of 14.2 μM and a mixed type of inhibition. The electrostatic potential map of V_{15} and other POMs were correlated with the enzyme activity inhibition. V_{15} also exhibited cytotoxicity against MDA-MB-231 (IC_{50} = 17.2 μM) and MCF-7 (IC_{50} = 15.1 μM) breast cancer cell lines. Using V_{15} concentrations equivalent to half and 1/4 of the IC_{50}, it was observed that MDA-MB-231 cell migration was reduced by 90 and 70%, after 24 h, respectively. Moreover, V_{15} caused morphological changes from fusiform to an epithelial-like (amoeboid) shape. Finally, V_{15} induced the increase in RIPK1, MLKL, and RIPK3 gene expression, up to 3, 10, and 15-fold, respectively, pointing out that the mechanisms of cell death in the triple-negative breast cancer cell line may occur by necroptosis.

Keywords: polyoxometalates; decavanadate; mixed-valence polyoxovanadates; P-type ATPases; Ca^{2+}-ATPase; electrostatic potential map; breast cancer; triple-negative breast cancer; MDA-MB-231; MCF-7

Academic Editors: Dinorah Gambino and Gonzalo Scalese

Received: 14 August 2025
Revised: 6 September 2025
Accepted: 9 September 2025
Published: 12 September 2025

Citation: Brito, B.R.; Camilo, H.d.S.; Cruz, A.F.d.; Ribeiro, R.R.; de Sá, E.L.; Camargo de Oliveira, C.; Fraqueza, G.; Klassen, G.; Aureliano, M.; Nunes, G.G. Mixed-Valence Pentadecavanadate with Ca^{2+}-ATPase Inhibition Potential and Anti-Breast Cancer Activity. *Inorganics* **2025**, *13*, 306. https://doi.org/10.3390/inorganics13090306

1. Introduction

Polyoxovanadates (POVs), an important subclass of polyoxometalates (POMs), are polyatomic oxide anions that contain vanadium in its highest oxidation states. Decavanadate, $[H_nV_{10}O_{18}]^{(6-n)-}$ (V_{10}), is the most extensively studied POV regarding its biological activity, such as antitumor and antibacterial activity, and is used in protein crystallography, serving as a model compound for understanding the interactions between POVs and proteins [1]. The potential of V_{10} as an antitumor agent has been explored with promising results, for example, for the hybrid compound Metformin-V_{10} that showed stronger

antiproliferative effects on melanoma cells [2]. Many of the in vivo and in vitro biological effects of V_{10} have been linked to inhibition of P-type ATPases [1].

Calcium ions are universal secondary messengers that play a vital role in the functioning of mitochondrial processes such as adenosine triphosphate (ATP) production, reactive oxygen species (ROS) generation, and apoptosis [3]. An imbalance in Ca^{2+} levels is associated with several diseases, including cancer, diabetes, Parkinson's disease, and Alzheimer's disease [4–6]. The Ca^{2+}-ATPase of the sarcoplasmic reticulum, found in muscle, is a transmembrane ion transporter. It is one of the most representative enzymes belonging to the family of P-type ATPases involved in cytosolic Ca^{2+} homeostasis. This enzyme is vital for the proper functioning of cells, and in the specific case of Ca^{2+}-ATPase, it regulates muscle contraction and relaxation [7]. Ca^{2+}-ATPase inhibitors have been used as drugs for cardioprotection, immunosuppression, and antitumor agents. The latter effect occurs due to the increase in cytoplasmic Ca^{2+} levels, which consequently activates apoptotic factors, leading to cell death [8,9]. As previously described, these P-type ATPases were considered one of the potential targets for POMs, which are expected to develop into the next generation of anticancer drugs that selectively target cancer cells [10]. Moreover, the calcium homeostasis dysfunction, a well-known hallmark of cancer, has recently been reviewed for its role in chemoresistance [11].

Recently, a POV with all vanadium centers in +V oxidation state, $PV_{14\,ox}$, was tested regarding its effect on U87 glioblastoma cells, and it was also reported to inhibit Ca^{2+}-ATPase and Na^+/K^+-ATPase in vitro and ex vivo, respectively [12]. Besides targeting these enzymes, also classified as P-type ATPases, POMs were also described to act as agonists of P2X receptors in hippocampal neuronal HT-22 cells, with the activation of metabotropic purinergic P2 receptors responsible for about 80% contribution to the cytosolic Ca^{2+} increase [13]. Therefore, by affecting cellular Ca^{2+} homeostasis implicitly, POMs might interfere with several physiological and pathological processes, among others [13,14].

Mixed-valence polyoxovanadates (MV-POVs) can adopt various structural patterns, including wheel and bowl-type structures, Lindqvist-type [15], and a range of pseudo-spherical, host–guest vanadium-oxido $\{V_{14}\}$, $\{V_{15}\}$, $\{V_{16}\}$, $\{V_{17}\}$, and $\{V_{18}\}$ clusters, with different combinations of +III, +IV, and +V oxidation states. Studies using Density Functional Theory, DFT, have demonstrated that in such compounds, the electrons in the aggregate tend to be uniformly distributed over all the vanadium centres [16]. The pentadecavanadates, $[X@V_{15}O_{36}]^{q-}$, where $X = Cl^-$, Br^-, and CO_3^{2-}, and net charge q = 4, 6, or 8, consist of fifteen edge-shared $\{O=VO_4\}$ square pyramids arranged in a pseudo-spherical structure with approximate C_{2v} symmetry, encapsulating a single anion. These cage-like MV-POVs have been studied for their magnetic and electrochemical properties and applied to build a wood-based solar evaporation generator that achieves 90% efficiency for water purification [17].

Although MV-POVs encompass the oxidation states most frequently observed under physiological conditions, their therapeutic potential remains comparatively underexplored in relation to other polyoxometalates [18]. Specifically, the $[(CH_3)_4N]_6[Cl@V^{IV}_8V^V_7O_{36}]$ (V_{15}) [19] has been evaluated in its interaction with different biological targets in the last 15 years (Figure 1). In studies developed by our research group, V_{15} showed a chemoprotective effect of pUC19 plasmid DNA of up to 70%, minimizing the action of potentially carcinogenic agents such as the alkylating agent diethyl sulfate. Moreover, *Escherichia coli* cultures have been used as a more complex cell model system, resulting in approximately 40% chemoprotection for V_{15} and $[I@V^{IV}_{12}V^V_6O_{42}]^{7-}$ ($V_{18}I$) [20]. Correlation with spectroscopic studies has suggested a relationship between stability in solution and chemoprotective performance, where MV-POVs containing encapsulated halides V_{15} and $V_{18}I$ have shown more promising results than V_{10} and those containing phosphate encapsulated [20]. The studies de-

veloped in vitro have enabled us to evaluate the reactivity patterns of MV-POVs in a controlled biological environment, thereby establishing structure-activity-reactivity relationships.

Studies involving ABC transporter P-glycoprotein showed that V_{15} can inhibit the multidrug resistance associated with this membrane transporter. Currently, the resistance to multiple drugs with different chemical structures and mechanisms of action is a major challenge in conventional cancer therapies [21]. Recently, it was demonstrated that V_{15} interacts with Chinese Hamster Ovary cells, decreasing the packing of membrane lipids and increasing signal transduction pathways mediated by the aggregation of the luteinizing hormone receptor (LHR) [22]. The LHR is a G-protein-coupled receptor that plays a key role in reproductive physiology in both males and females [22]. In addition, it was recently reported that a crystallographic structure of a model lysozyme, in which different MV-POV, including $[(H_2O)@V_{15}O_{36}]^{5-}$, non-covalently interact with enzyme surface residues [23]. Recently, the crystalline structure of a $Cl@V_{15}$-ferritin adduct was reported as obtained from a suspension containing $[V^{IV}O(acac)_2]$, where acac = acetylacetonato, and H-chain ferritin in basic medium, under mild conditions [24]. This physiologically relevant protein was involved in the spontaneous formation and stabilization of the mixed-valence $[Cl@V_{15}O_{36}]^{6-}$, containing 8V(IV): 7V(V), which corresponds to the classical polyoxidoanion described by Muller and used in this work, differing only in the cations. These achievements should encourage further research into mixed-valence cage-like chemistry and delve into their biological properties.

Among the few in vivo studies with POVs accessing anticancer activity, V_{10} prevented and suppressed tumor growth (B16-F10 melanoma allografted mice) in 70% [25]. A heterometallic Mo/V-POV reduced breast tumor growth in BALB/c female mice [26]. The V_{10} was evaluated for its toxicity to *Sparus aurata* fish [27], while V_{15} was assessed in mice through an acute 28-day repeated toxicity study. To our knowledge, no other POV has been studied so far, finding a moderated toxicity following a single oral dose of V_{15} from 25 to 2000 mg kg^{-1}, even after 14 days of exposure. However, repeated daily exposure over 28 days caused high toxicity at doses above 25 mg/kg, and V_{15} was classified as level 5 in the oral assay [28]. Taking all together, not only V_{15}, but also other compounds with physiologically accessible oxidation states of vanadium must be considered to better understand MV-POV chemistry, with a view to the safe future use of drugs based on vanadium.

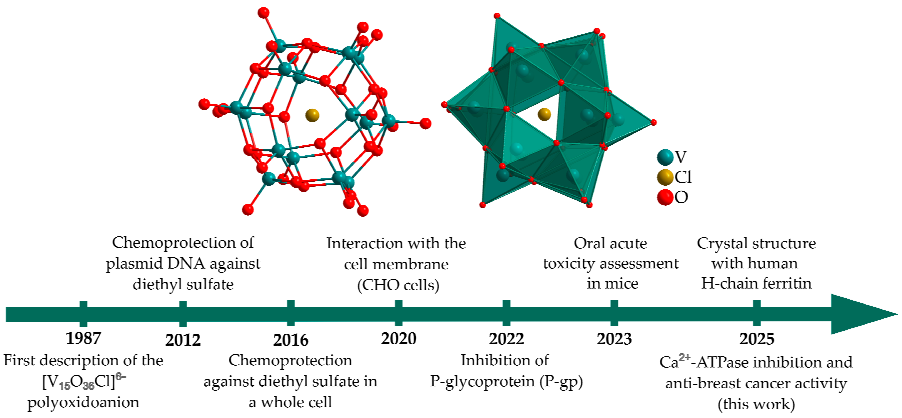

Figure 1. Timeline of the cage-like MV-POV $[(CH_3)_4N]_6[Cl@V_{15}O_{36}]$ (V_{15}), emphasizing its role in biological applications, with ball-and-stick and polyhedral representations (the cations were omitted for clarity) [19–22,24,28,29].

The previous studies motivated us to further explore the biological activities of V_{15} to analyze its anticancer potential. Breast cancer is the most common cancer and causes the highest mortality among women worldwide, and is subdivided according to molecular mechanisms and aggressiveness [30]. The metastatic disease, responsible for more than 90%

of cancer-related deaths, is defined by the ability of cancer cells to detach from the primary tumor and, through the bloodstream, invade nearby tissues, forming secondary tumors in different organs. The molecular classification of breast cancer subtypes mainly involves the estrogen and progesterone receptor genes (RE and RP, respectively) and the HER2 protein [31]. There are 4 molecular subtypes, with 70% of tumors classified as luminal A and B, characterized by the expression of hormone receptors RE and RP and negative for HER2 (Luminal A) or weakly positive for HER2 (Luminal B). Luminal subtypes are the least aggressive, with luminal B being more aggressive than luminal A. In order of aggressiveness, 15–20% are HER2 positive (overexpressing the HER2 protein) and 15% are triple negative (TNG), i.e., they do not have hormone receptors or overexpress HER2 [31]. Despite optimal systemic chemotherapy, fewer than 30% of women with metastatic breast cancer survive 5 years after diagnosis, and virtually all women with metastatic triple-negative breast cancer will ultimately die of their disease [32].

For luminal tumors, therapy uses tamoxifen (hormone therapy) or aromatase inhibitors, and for HER2 tumors, the monoclonal antibody trastuzumab (anti-HER2 antibody) is used. Advanced breast cancer, especially TNG, presents a highly metastatic profile and drug resistance. The lack of specific therapeutic targets means that TNG tumors are treated only with chemotherapy agents (e.g., doxorubicin and/or paclitaxel). However, chemotherapy agents present severe acute side effects ranging from vomiting and intense malaise to adverse effects such as cardiotoxicity, neurotoxicity, and neuropathy [33,34]. In this sense, vanadium compounds, including POVs, are promising chemotherapy agents, besides the well-known inorganic-based drugs containing cisplatin [35,36], as several studies have shown that they are active at different stages of carcinogenesis, such as prevention, therapy, and early diagnosis [37].

Nowadays, in breast cancer, we have found many research fields and/or perspectives such as cancer genomics, cancer therapy resistance, artificial intelligence tools, DNA repair and immunosurveillance, tumor microenvironment, clinical cancer biomarkers, non-invasive diagnostics, signaling in triple-negative breast cancer, chemotherapeutic agents for breast cancer, association with other cancer types, among many others [38]. Additionally, cancer research is conducted to discover new inorganic compounds, such as POMs, that combine inhibitory effects and/or reversal of drug resistance, as well as for breast cancer photothermal therapy using POMs-based nanoparticles [26,35,36,39].

The aim of this work is to pursue the studies of the putative biological activities of the mixed-valence pentadecavanadate, $[(CH_3)_4N]_6[Cl@V_{15}O_{36}]$ (V_{15}), analyzing the Ca^{2+}-ATPase inhibition potential and its anti-breast cancer activity in the luminal breast cancer cell line (MCF-7) and the TNG breast cancer cell line (MDA-MB-231). Specifically, in this work, we undertook the following tasks: (i) the evaluation of the V_{15} stability and speciation under the experimental conditions employed using ^{51}V NMR and UV/Vis spectroscopy; (ii) the determination of the IC_{50} value for inhibition of Ca^{2+}-ATPase activity, using a enzymatic couple assay; (iii) the determination of V_{max} and K_m kinetic parameters, regarding the native ligand ATP, using the couple enzymatic assay and the Lineweaver-Burk plot of Ca^{2+}-ATPase in the absence or presence of inhibitor for determination of the type of enzyme inhibition; (iv) comparison of the electrostatic potential map of $[V_{10}O_{28}]^{6-}$ (V_{10}), $[MnV_{13}O_{38}]^{7-}$(MnV_{13}), $[V^{V}{}_{14}O_{38}(PO_4)]^{9-}$ (PV_{14ox}) and also $[Nb_{10}O_{28}]^{6-}$ (Nb_{10}) with $[Cl@V^{V}{}_7V^{IV}{}_8O_{36}]^{6-}$ (V_{15}); (v) determination of the V_{15} IC_{50} values against MDA-MB-231 and MCF-7 cell lines, at 24 h; (vi) analysis of the effect of V_{15} in MDA-MB-231 cell migration; (vii) to verify V_{15} modulation of epithelial–mesenchymal transition (EMT) in MDA-MB-231 by cell morphology alteration; (viii) the putative mechanism of cell death induced by V_{15} searching for necroptosis and apoptosis.

2. Results and Discussion

2.1. Stability Studies

Although the characterization of POV structures in the solid state is important, understanding their behavior in solution is essential to identify the vanadium species present in equilibrium, which may include bioactive forms that contribute to the overall biological activity. It is known that the stability of POVs depends on the counter cation [40], the encapsulated anion [16], and the buffer or culture medium compositions used in the biological assay [41]. In the physiological medium, interaction of POVs with peptides and proteins may also change the nuclearity and oxidation state of the vanadium compound [42]. The stability study of V_{15} was already performed in solution containing DMEM medium (pH 7.4) [22], water (pH 6.3) [29], PIPES (pH 7.5) [29], and LB (Luria–Bertani) medium [20]. These correlations are essential for the rational selection of new biological applications.

Herein, the speciation of 1.0 mM V_{15} in enzymatic medium at pH 7.0 (25 mM HEPES, 100 mM KCl, 5.0 mM $MgCl_2$, 50 μM $CaCl_2$), and in RPMI medium (pH 7.4) after incubation at room temperature, was monitored by ^{51}V NMR (Figure 2). Spectra were also recorded in water for comparison. In water/D_2O and RPMI, NMR spectra were recorded at 0, 3, 10, 24, 48, and 72 h, reflecting the conditions used in the cellular viability assay. In the enzymatic medium, spectra were acquired at 0 and 1 h, aligning with the time course of the Ca^{2+}-ATPase inhibition assay.

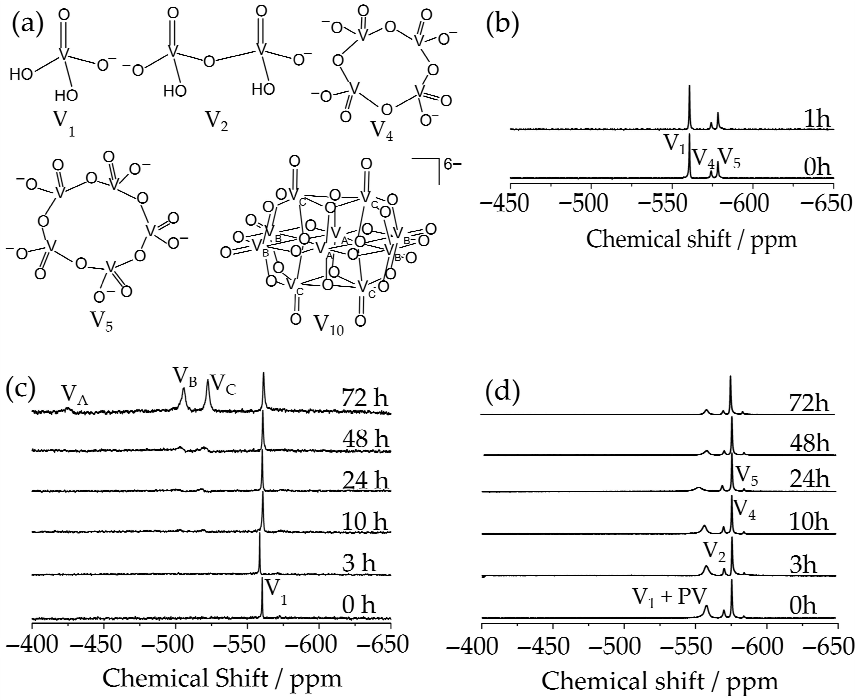

Figure 2. ^{51}V NMR spectra recorded at room temperature of 1.0 mM V_{15} solutions at different times. In (**a**) structure of the vanadium species. In (**b**), a freshly prepared solution in enzymatic medium and after incubation for 1 h; (**c**) water/D_2O (9:1), pH 6.3, and (**d**) in RPMI (pH 7.4). In (**c**,**d**), the spectra were registered from freshly prepared solutions and after incubation for 3, 10, 24, 48, and 72 h.

After dissolving V_{15} in H_2O, only a signal at δ –560 ppm was detected, attributed to the mononuclear $[H_2VO_4]^-$ complex (V_1), indicating that V_{15} hydrolyses partially [43]. Since V_{15} contains seven V(V) and eight V(IV) centers, the intact mixed-valence cluster was not detected by ^{51}V NMR. Over time, the concentration of vanadium(V) species increases, and after approximately 10 h, the signals characteristic of the three vanadium(V) environments of V_{10} appeared (Figure 2c) [43]. The intensity of these signals increased over time, with

isomeric shifts at—423 (V_A), –504 (V_B), and –522 (V_C) ppm, consistent with the protonated $[HV_{10}O_{28}]^{5-}$ species [43].

In enzymatic medium, the ^{51}V NMR of V_{15} reveals signals for V_1, $[H_2V_2O_7]^{2-}$ (V_2) and $[V_4O_{12}]^{4-}$ (V_4) at –560, –574 and –578 ppm, respectively (Figure 2a). The speciation of POVs in solution is strongly pH-dependent, with V_{10} forming predominantly under acidic environments. This explains why V_{10} forms upon V_{15} hydrolysis in water but does not form in neutral buffered solutions. Given that RPMI medium contains nutrients such as amino acids, phosphate, and glucose, which are capable of binding metal ions, a more complex speciation profile was expected. Indeed, NMR signals corresponding to oligovanadates V_2, V_4, and $[V_5O_{15}]^{5-}$ (V_5) at δ –585 ppm were observed (Figure 2d) during the time of the experiment. Additionally, the signal at δ –558 ppm of V_1 represents a combination of V_1 and a phosphate-vanadate (PV) complex (V_1 + PV), as these species rapidly exchange on the NMR timescale [22].

The electronic paramagnetic resonance (EPR) spectroscopy at X-band complements the ^{51}V NMR studies, as EPR detects the paramagnetic V(IV), while ^{51}V NMR detects V(V) species. The 1.00 mM freshly prepared solutions of V_{15} in water, enzymatic, and RPMI media at 77 K (Figure S1) gave weak broad lines compatible with those previously described for the mixed-valence polyoxidoanions [20,22,29]. Although some variations in the spectra can be observed over 72 h, the poor signal-to-noise ratio prevented detailed analysis. However, no resolvable hyperfine structure, characteristic of vanadium(IV) mononuclear species, was detected. These results reinforce V_{15} stability in different conditions and a possible oxidation of vanadium(IV) to vanadium(V) upon hydrolysis.

Additionally, the stability of V_{15} in enzymatic and RPMI medium was monitored using UV/Vis/NIR spectroscopy over a period of 168 h, and the results were compared with those registered for the aqueous solution (Figure 3). In the initial time, the spectra displayed a broad band centered at 950 nm assigned to a partially delocalized intervalence charge-transfer transition (IVCT, type II, V(IV)→V(V)) [44] characteristic of MV-POVs [29]. A second, higher-intensity band, starting at approximately 500 nm and extending to the ultraviolet region, was also observed, and attributed to ligand-metal charge transfers (LMCT, pπ (O, oxo) → d(V)). In the aqueous solution, some oxidation of V(IV) to V(V) occurred, causing a gradual reduction in IVCT absorbance. After 168 h, the V_{15} concentration had dropped to 46% of its initial value, as found by the calibration curve (Figure S2). The aggregate also undergoes partial hydrolysis, resulting in a mixture of V_{15}, V_1, and V_{10}, as suggested by NMR data along with the evolution of UV/Vis/NIR spectrum profiles and the change in the color of the solution from intense green to yellowish green. It is well known that the octahedral V(V) in V_{10} causes a bathochromic shift in the LMCT bands compared to V(V) in other geometries, and that this transition is responsible for the yellow color of the anion [45].

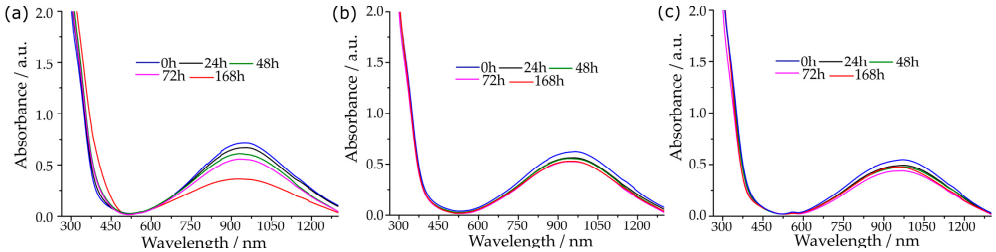

Figure 3. UV/Vis/NIR absorption spectra of V_{15} solutions at room temperature. The 1.0 mM solutions were incubated for 24, 48, 72, and 168 h: (**a**) in water; (**b**) in enzymatic medium; (**c**) in RPMI medium (pH 7.4).

Despite the speciation observed in NMR spectra in the initial time, V_{15} showed greater stability in the enzymatic medium containing HEPES pH 7.0, a buffer with a weak affinity for binding metal ions, in RPMI medium pH 7.4 (Figure 2b,d), reducing the MLCT band intensity by ca. 10% after 168 h. RPMI, on the other hand, has a composition rich in amino acids, including aspartate, that might interact with the POV and stabilize it or lead to redox reactions, depending on the conditions (temperature, pH, concentration, and ionic force of the medium). In the face of the above, V_{15} is more kinetically stable to hydrolysis for days under physiological conditions and is not completely oxidised or broken down into oligovanadates before exerting the biological effect reported here.

2.2. Inhibition of Ca^{2+}-ATPase

The effect of V_{15} on the activity of sarcoplasmic reticulum Ca^{2+}-ATPase from skeletal muscle was evaluated in vitro. V_{15} inhibited enzyme activity in a concentration-dependent manner, with a half-maximal inhibitory concentration (IC_{50}) value of 14.2 µM (Figure 4a).

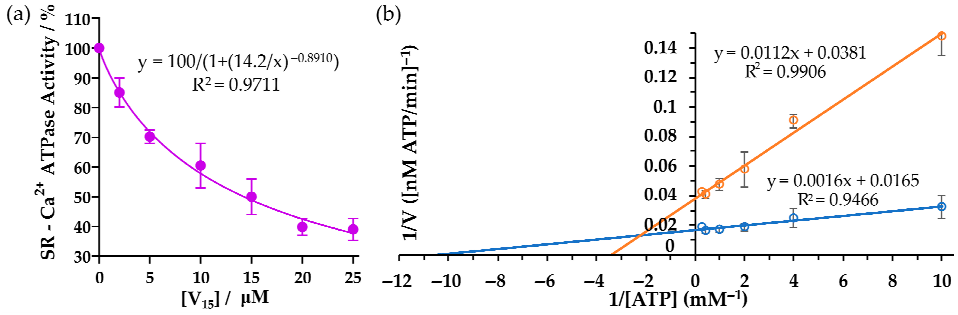

Figure 4. (**a**) Inhibition of Ca^{2+}-ATPase activity. (**b**) Lineweaver-Burk plot of Ca^{2+}-ATPase activity in the absence (blue) and in the presence (orange) of 15 µM de V_{15}.

Among other POVs, decavanadate (V_{10}) exhibits an IC_{50} of 15 µM [46]. In previously reported studies, the bicapped Keggin-type $[V^{V}_{14}O_{38}(PO_4)]^{9-}$ ($PV_{14\,ox}$) showed an IC_{50} of 5 µM [12], while $K_7MnV_{13}O_{38}$ (MnV_{13}) and $K_5MnV_{11}O_{33}$ (MnV_{11}) presented IC_{50} values of 31 µM and 58 µM, respectively [47]. Notably, both V_{15} and V_{10} carry the same net charge of −6 at physiological pH. Although their sizes and structures differ, the similarity in IC_{50} values may be attributed to their charge and the predominance of electrostatic interactions and hydrogen bonds with the target protein, as previously described for other POMs [48]. V_{15} solution at the IC_{50} concentration (15 µM) was incubated in the enzymatic medium for 60 min prior to measuring its inhibitory effect on Sarcoplasmic/Endoplasmic Reticulum Calcium ATPase (SERCA) hydrolysis activity. After incubation, V_{15} ATPase inhibitory activity was reduced to 42.4%, instead of 50% without incubation, indicating that the POV remains relatively stable in solution, even after 60 min. We emphasize that the IC_{50} values were determined during the first two minutes after the POV addition. In fact, no incubation was made with the POMs in the medium to prevent any decomposition. Therefore, it is suggested that V_{15} is the most probable species responsible for the observed inhibitory effects on the Ca^{2+}-ATPase, as described elsewhere for similar experimental conditions with other POMs [12,46–50]. On the other hand, if putative V_{15} decomposition into V_1 species occurs, it would lead to a lower inhibition potential activity for this ATPase, considering that the IC_{50} values for V_1 species were reported to be lower (IC_{50} = 80 µM) [49].

It was determined that V_{15} exerts a mixed-type inhibition on the ATPase activity, as evidenced by a decrease in V_{max} and an increase in K_m relative to the control measured by the slope and intercept of the double-reciprocal plot in Figure 4b. This suggests that V_{15} interacts with at least two distinct binding sites on the enzyme. In addition to the ATP-binding site, V_{15} may also bind to other domains of the Ca^{2+}-ATPase, regardless of whether

or not the enzyme is bound to its substrate. Mixed-type inhibition has also been reported for other POVs, such as PV_{14ox} and MnV_{13}. In contrast, V_{10} exhibits non-competitive inhibition with respect to ATP, suggesting mechanistic differences despite similar IC_{50} values between V_{10} and V_{15}. It is known that V_{10} binds to all conformational states of the enzyme—E1, E2, phosphorylated or not—whereas monomeric vanadate binds exclusively to the E2 conformation [49].

Furthermore, V_{10} can induce cysteine oxidation accompanied by the reduction of V(V) to V(IV), implying a potential role for V(IV) species in biological activity [51]. MV-POVs have already been observed, for instance, in lysozyme crystals [42]. X-ray structure studies have shown that $[(OH_2)@V_{15}O_{36}]^{5-}$ and $[(OH_2)@V_{15}O_{33}]^{+}$, both described as mixed-valence ($V^{V}{}_7/V^{IV}{}_8$), crystallize with lysozyme in a solution treated with monomeric vanadyl complex, $[V^{IV}O(acac)_2]$ (acac = acetylacetonato). The interaction with the protein occurs through hydrogen bonds with lysine, tyrosine, and arginine residues [42]. Moreover, $[V_{15}O_{33}(OH_2)]^{+}$ species was observed to form covalent bonds with the protein, where two POV oxygen atoms are replaced by those of aspartyl carboxylates, and a third is replaced by a glycine carbonyl oxygen. These interactions suggest that lysozyme structure provides a stabilizing environment for the V15-like-POVs [42,52].

These observations indicate that not only the surface charge, but also the POV specific structure and the presence of vanadium in the +IV oxidation state contribute to its interaction with Ca^{2+}-ATPase and the resulting inhibition of its enzymatic activity.

Electrostatic Potential (ESP) Map

The inhibition of Ca^{2+}-ATPase by POMs is frequently associated with their high negative surface charge and has been correlated with their charge density and size [48,53]. In fact, it was described that Preyssler-type anion $[NaP_5W_{30}O_{110}]^{14-}$ (P_5W_{30}) [50] and $[H_{10}Se_2W_{29}O_{103}]^{14-}$ ($Se_2W_{29}{}^{14-}$) with a similar charge density (q/m = 0.47 and 0.48, respectively) shows the highest POMs Ca^{2+}-ATPase inhibitory potential, respectively, IC_{50} = 0.37 and 0.3 μM whereas $[H_2P_2W_{12}O_{48}]^{12-}$ (P_2W_{12}) with a charge density of 1.00 presents a higher IC_{50} value (11 μM) [48]. Besides the charge of the POM, charge density, and size, other features may contribute to POMs' interactions with proteins and the inhibition of enzymatic activities. For example, the isostructural decavanadate (V_{10}) and decaniobate (Nb_{10}) with analogous structure, net charge, and approximately the same size but with different inhibition potential for the Ca^{2+}-ATPase activity (See Table 1 presented below), have been shown to present different binding sites for G-actin [51]. Thus, it was shown that V_{10} binds preferentially to the alpha binding site surrounded by Arg and Lys residues, being this the binding site of the natural substrate of the protein (ATP), whereas Nb_{10} binds to a binding site beta [54]. Besides this specific POV-actin interaction, several distinct modes of POVs' interactions with proteins have been recently described [54]. Regarding the Ca^{2+}-ATPase, V_{10} was found to crystallize in a highly positively charged groove formed by three protein domains [52], highlighting its ability to bind electrostatically to this region.

The Electrostatic Potential (ESP) map is a useful tool for examining the most probable sites of non-covalent interactions, such as electrostatic attractions and hydrogen bonds. The ESP is broadly used to visualize how the electrostatic potential varies across the surface of a molecule, and it also aids in analyzing intermolecular interactions based on electrostatic complementarity. ESP calculations were performed for V_{15} and for other selected discrete POVs that have been previously evaluated for their Ca^{2+}-ATPase inhibitory activity $[V_{10}O_{28}]^{6-}$ (V_{10}), $[Nb_{10}O_{28}]^{6-}$ (Nb_{10}), $[MnV_{13}O_{38}]^{7-}$ (MnV_{13}), which are expected to exist as deprotonated species under the enzymatic assay conditions [12]. The fully oxidized bicapped Keggin anion $[V^{V}{}_{14}O_{38}(PO_4)]^{9-}$ ($PV_{14\,ox}$) was also assessed despite its

low kinetic stability in aqueous solution at pH 7, because it coexists in equilibrium with oligovanadates in freshly prepared solutions [55].

Table 1. Surface maxima and minima of ESP (E_{max} and E_{min}, respectively), ΔE, and the volume enclosed by the calculated isosurface ($V_{isosurface}$ 0.001 e/bohr^3) and charge density (q/m).

Parameter	Nb_{10}	MnV_{13}	V_{10}	V_{15}	$PV_{14\ ox}$
IC_{50} μM	35	31	15	14.2	5
E_{max}/kcal mol^{-1}	−323.31	−350.29	−329.76	−306.01	−439.53
E_{min}/kcal mol^{-1}	−382.80	−468.82	−412.55	−354.20	−562.68
ΔE/kcal mol^{-1}	59.5	118.5	82.79	48.19	123.1
$V_{isosurface}$/Å^3	629.94	558.32	744.23	790.49	835.19
q/m	0.6	0.54	0.6	0.4	0.64
(q/m)/$V_{isosurface}$/10^{-4}	9.524	9.644	8.062	5.060	7.697

ΔE = E_{max} − E_{min}; q/m = is expressed as charge (q) of the POM divided by its number of metal atoms (m); $V_{isosurface}$ = volume of electron density in the POM.

For better comparison, all volume electron densities were represented as isosurfaces ($V_{isosurface}$, Figure 5), and are drawn using a continuous color gradient at the same electrostatic potential scale. All values on the isosurfaces are negative, with the most electron-rich areas in red, indicating regions of highest attraction for a positively charged species or ions. The blue areas represent the less negative potential values, while the green regions indicate intermediate electron-rich areas. Except for the heterometallic MnV_{13}, the most negative electrostatic surface potential values of the POMs are localized in the vicinity of the doubly and triply bridging oxygen atoms, while the terminal oxygen atoms exhibited the least negative electrostatic potential. For MnV_{13}, the most negative potentials are positioned in the centre of the aggregate.

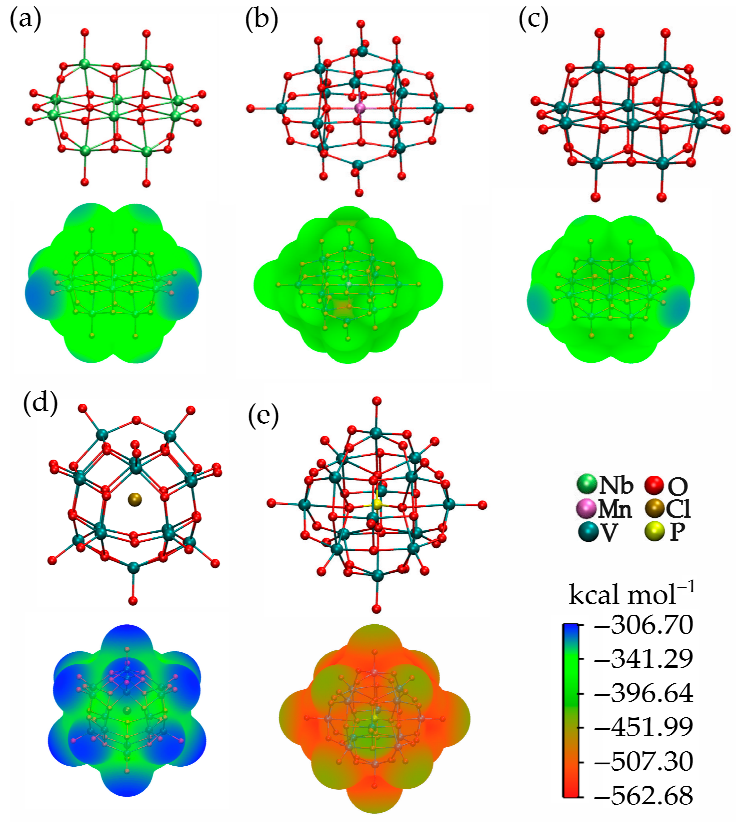

Figure 5. Ball and stick structures and ESP map of the anions (**a**) $[Nb_{10}O_{28}]^{6-}$ (Nb_{10}) (**b**) $[MnV_{13}O_{38}]^{7-}$ (MnV_{13}) (**c**) $[V_{10}O_{28}]^{6-}$ (V_{10}) (**d**) $[Cl@V^{V}{}_{7}V^{IV}{}_{8}O_{36}]^{6-}$ (V_{15}) (**e**) $[V^{V}{}_{14}O_{38}(PO_4)]^{9-}$ ($PV_{14\ ox}$).

To shed light on the factors involved in the Ca^{2+}-ATPase inhibitory activity promoted by POVs, some molecular and electrostatic features were attempted to correlate with IC_{50} values depicted in Table 1. The relative order for both E_{max} and E_{min} is V_{15} < Nb_{10} < V_{10} < MnV_{13} < $PV_{14\,ox}$, while the IC_{50} order is Nb_{10} < MnV_{13} < V_{10}~V_{15} < $PV_{14\,ox}$. The analysis of the results reveals two important parameters: the surface maxima and minima values in ESP (E_{max} and E_{min}), and the volume enclosed by the isosurface ($V_{isosurface}$).

Regarding the border inhibitors, $PV_{14\,ox}$ shows the most negative E_{min}, the highest ΔE value (123 kcal mol^{-1}), and the biggest $V_{isosurface}$ of 835.19 $Å^3$, being the most nucleophilic POV and exhibiting the strongest inhibition of Ca^{2+}-ATPase (Table 1). On the other hand, the poorest inhibitor, Nb_{10}, presents E_{min} of—382.80 kcal mol^{-1} and a ΔE value of only 59 kcal mol^{-1}; moreover, its $V_{isosurface}$ is 25% smaller than the $PV_{14\,ox}$ one. The E_{max} and E_{min} for V_{10} are slightly more negative than those for Nb_{10}, but its $V_{isosurface}$ being 18% larger might be associated with its inhibitory activity, which is 1.75 times more potent. The MnV_{13}, in turn, exhibits the second-lowest Emin value, but its IC_{50} is comparable to that of Nb_{10}. Here, the impact of the volume is significant because it showed the lowest $V_{isosurface}$, i.e., 29% and 33% smaller than V_{15} and $PV_{14\,ox}$.

The V_{15} is a key aggregate to demonstrate the correlation between the Ca^{2+}-ATPase activity with the ESP and the $V_{isosurface}$, because even showing the lowest E_{max}, E_{min}, and a ΔE of only 48 kcal mol^{-1}, its IC_{50} value is close to the V_{10} (15 and 14.2 μM). The $V_{isosurface}$ calculated for V_{15} is only 5.9% bigger than V_{10} and 5.4% smaller than $PV_{14\,ox}$, but considerably higher than Nb_{10}, achieving 25%. These results showed that, despite their structural differences and variations in vanadium oxidation states, V_{10} and V_{15} display similar availability of negative charge to participate in electrostatic interactions with the expected binding site of this enzyme [48]. However, the relationship between delocalization and electron density distribution in ESP is not straightforward, and there are still few systematic structural studies with mixed valence POVs to trace a linear correlation. As can be observed in Table 1, V_{15} presents a charge density (q/m) of 0.40. It was reported that POMs with moderate charge density (q/m = 0.33) interact strongly with protein surfaces due to a process named chaotropic effect [56]. It was suggested that this chaotropic effect contributes to a structure–activity relationship for the affinity of POMs towards proteins [56]. Still, further studies are needed to unravel at the molecular level the POMs features that correlate with specific biological activities.

2.3. Inhibition of Cell Viability in Breast Cancer Cells

The MTT assay was performed to evaluate cell viability using V_{15} in the non-tumorigenic, human mammary epithelial cell line (HB4a), luminal breast cancer cell line (MCF-7), and the triple-negative breast cancer cell line (MDA-MB-231). The cells were initially introduced into the wells to allow cell adhesion for 2 h, followed by the addition of increasing amounts of V_{15} (Figure S3). The results of cell viability inhibition of the cell lines treated with V_{15} showed a dose-dependent effect for the three cell lines, with an IC_{50} value of 1.02 μM for HB4a, 15.1 μM for MCF-7, and 17.2 μM for MDA-MB-231 (Figure 6 and Table 2). The IC_{50} value for luminal breast cancer cells was 16 times more potent than the commercial drug 5-fluorouracil under similar conditions (24 h, RPMI) [57].

Table 2. IC_{50} values determined for V_{15} regarding Ca^{2+}-ATPase inhibition, breast cancer cell lines (MCF-7 and MDA-MB-231), and normal breast cell line (HB4a) viabilities, after 24 h of incubation.

Assay	IC_{50} (μM)
Ca^{2+}-ATPase	14.2
HB4a	1.02
MCF-7	15.1
MDA-MB-231	17.2

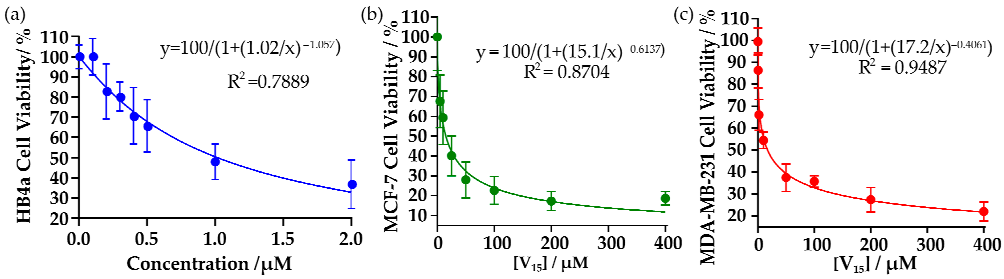

Figure 6. Evaluation of the cytotoxic effect on (**a**) HB4a, (**b**) MCF-7, and (**c**) MDA-MB-231 cell lines at different concentrations of V_{15} at 24 h. The graphs show the dose–response inhibition (IC_{50} determination) for all the cell lines, with the R-squared and linear curve fitting.

The non-tumorigenic cell line showed higher sensitivity to V_{15} compared to the two cancer cell lines, indicating that the POV does not exhibit selectivity regarding this experimental model. Despite the lack of selectivity, in our previous studies with V_{15} using peripheral blood mononuclear cells (PBMC), an IC_{50} value of 12.9 µM was determined in RPMI after 48 h [28]. These data, along with early toxicity studies in mice, may guide future in vivo research when focusing on the urgent need to develop new therapies for the triple-negative breast cancer subtype. In such studies, a V_{15} concentration in the order of 1.0 µM (see Figure S2) would be reasonable, because it produced a cytotoxic effect of approximately 30–40% on MDA-MB-231 cells.

The IC_{50} value of V_{15} in MCF-7 and MDA-MB-231 cell lines was selected to monitor cell viability over 24, 48, and 72 h. The graphs presented in Figure S4 demonstrate that the POV is a time-dependent potent inhibitor of cell growth in both cell lines, corroborating the value determined for the IC_{50} after 24 h of incubation. The time curve showed a significant decrease in the viability of MDA-MB-231 cells after incubation, with only 45.4% (24 h), 15.3% (48 h), and 8.3% (72 h) of cells remaining alive. Similar results were observed with MCF-7, showing 64.3% (24 h), 12.1% (48 h), and 3.03% (72 h). Therefore, V_{15} showed a cumulative effect in the interference of cell viability over time.

The IC_{50} values obtained for V_{15} in the MCF-7 and MDA-MB-231 cell lines are promising, as they are lower than those found in the literature for other polyoxovanadates. For MCF-7 cells, a literature POV hybrid covalently bonded to amino acid esters, $[V_6O_{13}\{(OCH_2)_3C_{10}H_{14}O_5\}_2]^{2-}$, exhibited a cytotoxic effect (IC_{50} = 53.01 µM) twice as strong as that of the traditional commercial drug 5-fluorouracil, in DMEM at 48 h [58]. Two decavanadates with betaine showed anticarcinogenic activity against MCF-7 cells at 24 h, with IC_{50} values close to 200 µM [59] while the super-Keggin MV-POV $[(H_2O)@V_{18}O_{42}]^{12-}$ ($H_2O@V_{18}$) presented IC_{50} values of 45.95 µM and >500 µM for 24 h, respectively [60]. According to spectroscopic studies, V_{15} is stable in RPMI medium, suggesting that the activity could be attributed to this MV-POV. To the best of our knowledge, no speciation studies are available for $H_2O@V_{18}$. The $H_2O@V_{18}$ presents the lowest cytotoxic effect, being approximately 3 and 30 times less potent than V_{15} for MCF-7 and MDA-MB-231 cells, respectively.

2.4. Inhibition of Cell Migration Using the Wound Healing Assay in MDA-MB-231 Cell Line

The Wound Healing assay is a simple method used to study cell migration. Reducing migration is desirable for a therapy that aims not only to diminish a tumor but also to delay or even prevent metastasis. The MDA-MB-231 cell line exhibits mesenchymal characteristics (fusiform shape), which is indicative of its migratory and invasive potential [61,62]. The cancer cells were treated with V_{15} at concentrations of 8.60 and 4.30 µM, equivalent to half and a quarter of the IC_{50} value, and the wound area was photographed after removing non-viable cells. Figure 7a displays selected images where, in the control, the typical

migration of the cell line over the scratch is observed. In both samples treated with V_{15}, the wound remained open, indicating that cell migration was impaired.

The wounds in the wells containing cells treated with both concentrations of V_{15} for 24 h were compared with the wounds of the control (non-treated cells) incubated for 24 h (Figure 7b). In the control samples, the wound area remained open by only 13%. For V_{15}, a dose-dependent cell migration was observed after 24 h, and consequently, the gap area remained 66% and 86% open for the lower and higher concentrations, respectively. Similar results were reported for decavanadate with tetra-(benzylammonium), which also inhibited cell migration of MDA-MB-231 at concentrations of 0.70 and 2.8 μM [63].

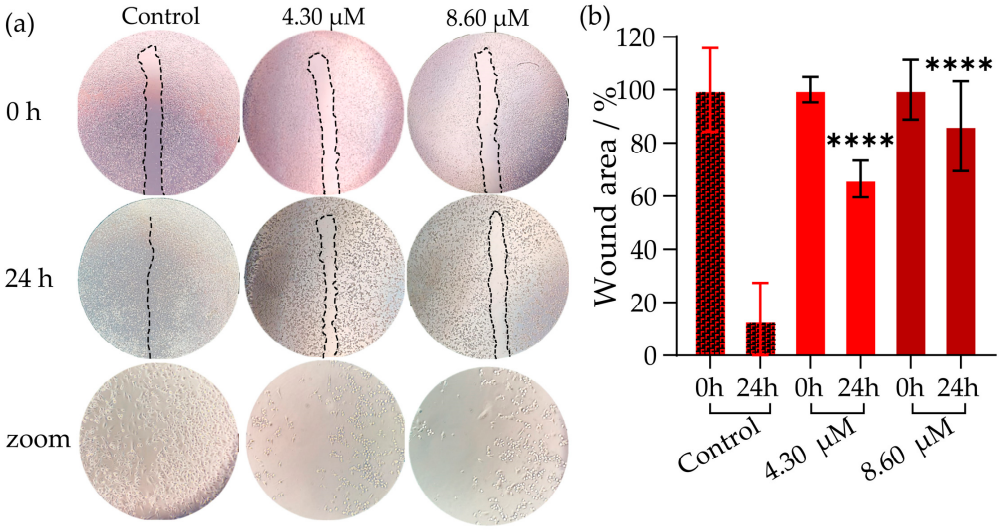

Figure 7. Inhibition of cell migration as analyzed by the Wound Healing Assay in the MDA-MB-231 cell line without treatment (negative control) and treated with V_{15} for 0 and 24 h. (**a**) Selected photos of cell migration over the wound, from a total of 6 repetitions. The zoom is related to the wound area. (**b**) The graph was generated by taking six images in each condition, with the aid of ImageJ.JS 1.53m software [64]. The asterisks indicate the statistical treatment for six repetitions compared to the control at 24 h. **** means $p < 0.001$. The bars represent the standard deviation.

2.5. Scanning Electron Microscopy (SEM Images) in MDA-MB-231 Cell Line

SEM analysis was performed on the MDA-MB-231 cell line at the same concentrations as those used in the Wound Healing assay (4.30 and 8.60 μM). The SEM images showed cells with a fusiform shape, characteristic of this mesenchymal subtype of triple-negative cell line (Figure 8a), which changed to a more epithelial-like (amoeboid) morphology (Figure 8b,c). This morphology is generally related to a lower migratory capacity, which corroborates the cell migration assays. Finally, the microvesicles that appeared after treatment with the highest dose of V_{15} might be associated with the beginning of the cell death process. These morphological changes in the cells may be related to interactions with the cytoskeleton and possibly with the actin [65].

A process that is related to the progression of the disease to the metastatic form is called epithelial–mesenchymal transition (EMT). EMT is a reversible process, transitioning from epithelial to mesenchymal cells through a change in morphology. EMT occurs naturally in several processes, such as wound healing and embryonic development. However, when associated with the formation of fibroblasts (tissue regeneration, trauma, or inflammation), it can cause fibrosis and organ damage. When in neoplastic cells, there is an increase in cell proliferation and invasive and metastatic phenotypes, increasing the malignancy and aggressiveness of the disease [65]. The EMT phenotypical alteration involves genetic and epigenetic modifications in cancer cells when they initiate the metastasis process. Here,

we observed a potential reverse process (mesenchymal–epithelial transition), indicating that V_{15} can switch off one of the most important hallmarks of cancer, thereby reducing the mechanism of progression to metastatic moving cells [65]. However, assays carried out at concentrations up to 1.0 μM of V_{15} caused only minor changes in cell morphology (Figure S5).

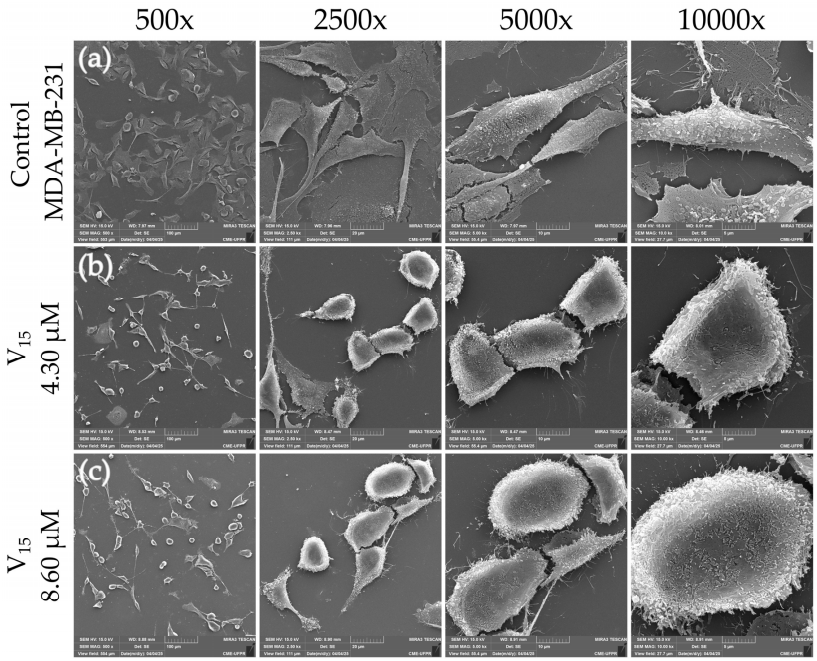

Figure 8. SEM images for V_{15} in MDA-MB-231 cell line, at magnifications of 500×, 2500×, 5000×, and 10,000× for (**a**) control; (**b**) concentration of 4.30 μM, and (**c**) 8.60 μM.

2.6. Gene Expression in MDA-MB-231 Cell Line

There are three classic mechanisms of cell death: apoptosis, necrosis, and necroptosis. Apoptosis is a programmed and "organized" cell death, essential for the development and homeostasis of the organism, and it does not trigger an inflammatory response. It is characterized by cell contraction and formation of apoptotic bodies, and since the cell contents are not released into the bloodstream, there is no inflammatory response. This mechanism can be triggered by internal signals, such as DNA damage or cell death signalling [66]. Necrosis is an unprogrammed cell death, usually triggered by injury, anoxia, or extreme tissue damage. Unlike apoptosis, it is an inflammatory process that results in the release of cellular contents into the bloodstream. It is characterized by cell swelling and rupture of the plasma membrane, leading to the release of cellular contents and the consequent inflammatory response. This mechanism can be caused mainly by a lack of blood supply [66].

Necroptosis is a cell death that resembles classical necrosis in morphology; however, it is a programmed inflammatory cell death. Unlike necrosis, it depends on a signaling pathway mediated by kinases called RIPK1 and RIPK3, with the pseudokinase MLKL acting as its effector molecule [66]. It is characterized by the controlled rupture of the plasma membrane and the release of cellular contents, but with some regulation compared to necrosis [66].

Based on the results presented above for the POVs, it was decided to investigate the cell death mechanism only for V_{15} in the MDA-MB-231 cell line, since it alters cell morphology, which may indicate interaction with the membrane and the triggering of processes inside the cell. The selected genes were those related to the mechanisms of apoptosis (*BCL2*, antiapoptosis; *TP53*, apoptosis mediated by DNA damage; *CASP8*, apoptosis via extrinsic

pathway; and *BAX*, pro-apoptosis), and necroptosis (*RIPK1*, *MLKL*, and *RIPK3*). The graphs of relative gene expression compared with control without treatment and normalized by *GAPDH* constitutive gene (Figure 9) showed that those referred to necroptosis mechanism, *RIPK1*, *MLKL*, and *RIPK3*, increased 3, 10, and 15-fold, respectively (Figure 9a). The expression of these genes indicates that one of the mechanisms of cell death caused by V_{15} in the TNG breast cancer cell line may occur by necroptosis. On the other hand, no statistically significant effect on the general apoptosis mechanism could be related to V_{15} in this model (Figure 9b).

Interaction with V_{15} can trigger the necroptosis pathway, signaled by the activation of the *RIPK3*, *RIPK1*, and *MLKL* genes, which are factors involved in the formation of the necrosome, activated when caspase inactivation or inhibition occurs. The necrosome, along with other factors, migrates to the cell membrane, causing rupture and leakage, leading to cell death [67]. Some studies with POMs confirm that this class of compounds can cross the cell membrane of cancer cells, localizing itself within the cytoplasm; however, the mechanism of action of POMs has not yet been thoroughly explored [68–73]. About forty years ago, Yamase performed the first study on the mechanism of POMs in cancer cells [74]. The proposed mechanism involves the reduction and reoxidation of POM, as well as of the cellular components of the electron transport chain, which can inhibit the formation of ATP, leading to cell death by apoptosis [74]. This proposed mechanism is based on a series of studies that suggested that the cytotoxicity of bioactive POMs directly relates to their redox potential; however, other factors, such as size, structure, and composition, also significantly influence the activity of POMs against cancer cells [10].

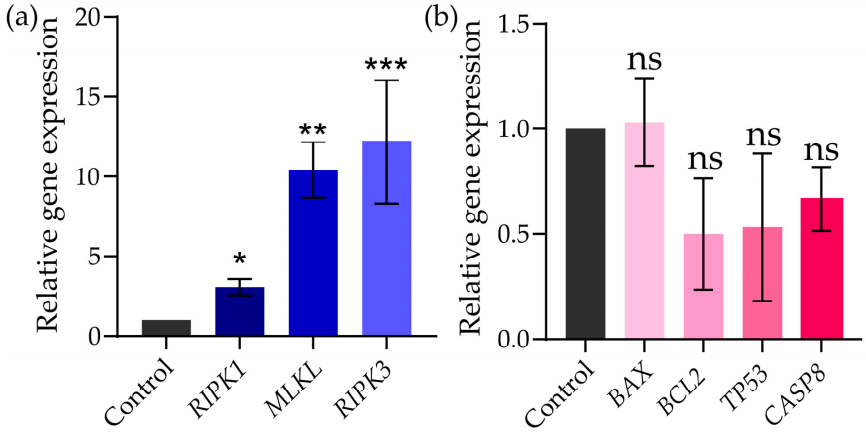

Figure 9. Evaluation of relative gene expression in the MDA-MB-231 line treated with 17.2 µM of V_{15} for 48 h. (**a**) Relative necroptosis gene expression and (**b**) relative apoptosis gene expression, compared to the constitutive gene *GAPDH*. The statistical treatment is compared to the control, ns (non-significant), * $p < 0.01$; ** $p < 0.001$; *** $p < 0.0001$.

POMs might affect cancer cells through several mechanisms, including the ones referred above, such as inducing apoptosis and affecting bioenergetics processes, but other mechanisms were described, such as interfering with DNA replication and gene expression, cell cycle arrest, generating reactive oxygen species (ROS), disrupting membrane transports, and/or inactivating essential enzymes within cancer cells [10,75]. Of course, those specific mechanisms for anticancer activity might depend on the POM's structure and composition in order to selectively target cancer cells and reduce toxicity to healthy cells. When comparing and sorting the cell viability IC_{50} values in ascending order for 20 human cancer cell lines tested for different types of POMs, the first polyoxovanadates (POVs), polyoxomolybdates (POMos), polyoxopaladates (POPds), and polyoxotungstates (POTs) [75]. When comparing clinically approved drugs and POMs, in many cases, better

results were observed for POMs in relation to the drugs [75]. Therefore, POVs such as V_{15} could become in the future an alternative to existing drugs in cancer therapy [75].

Alterations in calcium levels related to cell death by necroptosis have recently been revised, and it has been proposed that classical necroptosis is mediated by death receptors that work in synergy with caspase inhibitory signals [76]. However, a non-classical model of necroptosis has emerged. Based on the argument that cytosolic calcium signaling can drive the necroptotic mode of cell death in both dependent/independent receptor mechanisms when the cytoplasmic calcium levels are strictly related. Here we have found an inhibition of Ca^{2+}-ATPase activity and a putative correlation with a decrease in cell proliferation, a phenotypic switch from mesenchymal to epithelial, and cell death by necroptosis. More detailed studies are in progress to clarify this probably new mechanism of drug interaction with promising therapeutic future intervention [76].

3. Materials and Methods

3.1. Generalities

The synthesis reactions were carried out in air, in deionized water (ultrapure water, resistivity less than 3.5 $\mu S \cdot cm^{-1}$ at 25 °C). All the chemicals purchased were of reagent grade and were used without further purification. Roswell Park Memorial Institute (RPMI) medium and fetal bovine serum (FBS), both from Thermo Fisher Scientific (Waltham, MA, USA); 4-(2-hydroxyethyl)1-piperazine ethane sulfonic acid (HEPES) from Sigma-Aldrich (St. Louis, MO, USA); 3-(4,5-dimethyltiazol-2-yl)-2,5-diphenyl-tetrazolium bromide (MTT), sodium cacodylate, glutaraldehyde, and osmium tetroxide were provided by Merck (Darmstadt, Germany). The AllPrep DNA/RNA Mini Kit (Qiagen, Hilden, Germany), SuperScript IV from Invitrogen (Walthan, MA, USA), and SYBR Green Power Master Mix from Applied Biosystems (Foster City, CA, USA) were used as received.

Powder X-ray diffractogram (PXRD) was registered on a Shimadzu XRD-6000 equipment (Kyoto, Japan), with Cu-Kα radiation (λ = 1.5418 Å) using silicon powder as an internal standard, using a voltage of 40 kV, current of 30 mA, and scan speeds of $0.02^{\circ}s^{-1}$ (at 2θ). The ^{51}V NMR spectra were recorded using a Bruker Avance 400 MHz (9.4 T) equipment (Ettlingen, Germany) , equipped with a direct detection multinuclear probe (5 mm). The spectra were acquired at 303 K with 500 µL of each sample solution, using 90° pulses. The spectra were registered with 2048 scans, with a recycle delay of 0.100 s and acquisition times of 0.218 s, along a spectral window of 714 ppm (+ 50 ppm to −650 ppm) with a ^{51}V core acquisition frequency of 105.25 MHz. Electron Paramagnetic Resonance spectra were recorded in an X-band Bruker ELEXSYS E-500 spectrometer (Ettlingen, Germany) from solution frozen at 77 K. The spectra were referenced using pure $VOCl_3$ in a capillary (external reference), fixing the signal at 0.00 ppm. UV-vis/NIR spectra were recorded on a PerkinElmer LAMBDA 1050 UV-Vis/NIR spectrophotometer (Waltham, MA, USA) equipped with three PMT/InGaAs/PbS detectors at room temperature in a wavelength range of 265–1300 nm. Scanning Electron Microscopy (SEM) analyses were performed using a TESCAN VEGA3 LMU equipment (Brno, Czech Republic) , with a resolution of 3.0 nm, at magnifications ranging from 500× to 10,000×.

Synthesis and Stock Solution of V_{15}

The $(Me_4N)_6[Cl@V_{15}O_{36}]$, $V_{15,}$ was synthesized following the procedure described in the literature [29] and in the Supplementary Material. A detailed scaled-up synthesis was described for some of us in reference [28]. IR spectra were registered for a freshly synthesized sample, after two months and two years of aging. Main bands in IR spectrum (Figure S6) of dark green crystals: ν_{as} and ν_s (CH_3) weak bands at 3024 and 2952 cm^{-1} respectively, strong δ_{as} and $\delta_s(CH_3)$ absorptions at 1485 cm^{-1} and 1446 cm^{-1} respectively,

and ν(V=O) at 983 cm^{-1}; ν(V−O−V) at 580, 660 and 725 cm^{-1}. The diffraction peaks at angles 2θ of 7.4, 8.6, 15.4, 17.6, 19.9, 22.3, 23.1, 25.7, 26.7, 27.2, 30.7, 32.8, 33.2, 41.2 and 41.7° (Figure S7) are in good agreement with those previously reported, confirming that the solid was isolated free of the fresnoite-type oxide $(NH_4)_2V_3O_8$, a common insoluble byproduct in the synthesis of mixed-valence POVs [28].

New data on V_{15} stability in solid state over a period of 2 years were obtained by the infrared spectroscopic analysis, indicating that this MV-POV remained stable for a long time of storage (Figure S6). Stock solutions of V_{15} were prepared at a concentration of 1.0 mM (pH 4.67) in heated water, considering a molecular weight of 1820.42 g mol^{-1} to yield a green solution. Freshly prepared solutions were used in all experiments to prevent oxidation of the vanadium. The aqueous solution was diluted in RPMI culture medium or enzymatic medium to the desired concentration specified in each biological assay. The enzymatic medium contained: 25 mM HEPES (pH 7.0), 100 mM KCl, 5 mM $MgCl_2$, and 50 μM $CaCl_2$.

3.2. Spectroscopic Studies in Solution

The vanadium species formed in a 1.0 mM V_{15} solution were determined using vanadium nuclear magnetic resonance (^{51}V NMR) spectroscopy. For sample preparation, 450 μL of 1.11 mM stock solution of V_{15} in water, RPMI pH 7.4 (9:1), without the addition of fetal bovine serum or enzymatic medium, received 50 μL of D_2O, to render a final concentration of 1.0 mM. The spectra in aqueous solution and in RPMI medium were recorded at several points (0, 3, 10, 24, 48, and 72 h) to determine whether there were changes in the speciation during the time of the cellular cytotoxicity experiment. The spectra in the enzymatic medium were recorded at 0 h and 1 h.

Ultraviolet, visible, and near-infrared (UV/Vis/NIR) spectroscopy was used to follow the consumption of V_{15} at times of 0, 3, 10, 24, 48, 72 and 168 h, measuring the absorption band from 265 to 1300 nm in a PerkinElmer LAMBDA 1050 UV/Vis/NIR spectrophotometer (Waltham, MA, USA) equipped with three PMT/InGaAs/PbS. All spectra were recorded at ambient temperature in water, RPMI, and enzymatic media. A 1.0 mM solution of V_{15} in each condition was incubated for up to 168 h at 25 °C, and the spectrum was recorded at 24 h intervals. Due to the high molar absorptivity of V_{15}, all samples had to be diluted to 0.020 mM prior to analysis to guarantee a detection within the linear range.

3.3. Computational Methods

The crystallographic data for the selected polyoxovanadates were available in the Cambridge Crystallographic Data Centre with CCDC numbers 722216 $[Nb_{10}O_{28}]^{6-}$ [77], 1610770 $[MnV_{13}O_{38}]^{7-}$ [78], 1839623 $[V_{10}O_{28}]^{6-}$ [79], 794586 $[Cl@V^{V}{}_7V^{IV}{}_8O_{36}]^{6-}$ [29], 1886317 $[V^{V}{}_{14}O_{38}(PO_4)]^{9-}$ [12]. The structure of V_{10} was subject to geometric optimisation after removal of hydrogens, using Density Functional Theory (DFT) with the WB97X-D3 functional [80,81] and DEF2-TZVP basis set [82], utilising ORCA 5.0.4 software [83]. Electrostatic potential (ESP) map calculations were conducted using Multiwfn 3.8 software with an isosurface defined as 0.001 e/$bohr^3$ [84–86]. The isosurfaces were rendered using the VMD—Visual Molecular Dynamics 1.9.3 software [87]. For $[Nb_{10}O_{28}]^{6-}$, the wave function was calculated using the relativistic Hamiltonian Douglas–Kroll–Hess (DKH), with the basis SARC-DKH-TZVP for niobium and DKH-def2-TZVP with the auxiliary set SARC/J for the oxygens [88].

3.4. Inhibition of Ca^{2+}-ATPase Activity by V_{15}

Isolated sarcoplasmic reticulum (SR) vesicles prepared from rabbit skeletal muscles as described elsewhere [46] were suspended in 0.1 M KCl, 10 mM HEPES (pH 7.0), diluted 1:1 with 2.0 M sucrose, and frozen in liquid nitrogen prior to storage at −80 °C.

The activity of Ca^{2+}-ATPase and its inhibition of the POV solution were measured spectrophotometrically by monitoring the change in absorbance at 340 nm at room temperature, both in the absence (100% activity) and in the presence of several concentrations of V_{15} (2.0, 5.0, 10, 15, 20, and 25 μM) for determination of IC_{50} (Figure 2a), for determination of the type of inhibition (Figure 2b) the activity was measured without inhibitor and with inhibitor (V_{15} at 15 μM) using increasing ATP concentrations (0.10 mM, 0.25 mM, 0.50 mM, 1.0 mM, 2.5 mM, and 3.75 mM).

The measurements were performed using the coupled enzyme pyruvate kinase/lactate dehydrogenase assay, as described elsewhere [46]. Aqueous stock solutions of V_{15} were prepared prior to use at 1.0 mM in water. The reaction medium contained the following: 25 mM HEPES (pH 7.0), 100 mM KCl, 5 mM $MgCl_2$, and 50 μM $CaCl_2$. For the coupled enzyme assay, the following components were added: 0.42 mM phosphoenolpyruvate, 18 IU lactate dehydrogenase, 7.5 IU pyruvate kinase, 0.25 mM NADH, and 2.5 mM ATP. The POV solution was added to the assay medium, and the experiment was initiated immediately after the addition of SR vesicles containing the Ca^{2+}-ATPase (10 μg mL^{-1}), and the absorbance was followed for about 1 min to measure the basal activity. Subsequently, 4% (*w*/*w*) calcium ionophore A23187 was added to the cuvette, and the decrease in absorbance was recorded for 3 min (uncoupled ATPase activity). ATPase activity and inhibition were calculated based on the rate of absorbance decrease per minute in the absence and presence of V_{15}. Data are presented as means standard deviation (± SD). The results represent the average of triplicate experiments. The inhibitory effect of V_{15} was expressed as the IC_{50} value, defined as the concentration of V_{15} that induces 50% inhibition of Ca^{2+}-ATPase activity.

3.5. Cell Culture

The human breast cancer cell lines, MDA-MB-231 and MCF-7, were provided by the ATCC (American Type Culture Collection) from Manassas, VA, USA). The cells were cultivated in RPMI 1640 medium supplemented with 10% FBS at 5% CO_2 and 37 °C in a humidified atmosphere.

3.6. MTT Assay

The MDA-MB-231 and MCF-7 cells were cultured in RPMI medium containing approximately 5×10^3 cells/well in a 96-well plate. The V_{15} was solubilized in water and included after 2 h of cellular adhesion. After incubating for 24 h, the in vitro cytotoxicity was measured by the MTT assay [89], and the results were analyzed in a MULTISKAN SkyHigh multiplate spectrophotometer (Vantaa, Finland) at a wavelength of 540 nm. IC_{50} values were calculated using GraphPad Prism 7 Software for Windows. Cell viability values were expressed as arithmetic means, with standard deviation calculated considering three independent experiments. Differences between multiple groups and controls were detected by one-way ANOVA followed by Tukey's multiple comparisons test. A value of $p < 0.05$ was considered statistically significant [90].

3.7. Cell Migration by Wound Healing Assay

The MDA-MB-231 cell line was cultured in 6-well plates with the addition of 6×10^5 cells per well. After cells confluence, FBS was removed for 4 h, and using a tip, a straight opening through the cell monolayer was made [91]. V_{15} (4.30 and 8.60 μM) was added, and the cultures were incubated with RPMI medium containing 1% FBS. Each well was washed 3 times with 1.0 mL of PBS 1x to remove the dead cells. The area of the opening in the cultures was photographed using an inverted microscope at 0, 24 h, and the wound area was measured using ImageJ® 1.53m software to analyze cell migration.

3.8. Scanning Electron Microscopy (SEM) Images

The preparation of cell line samples for SEM was carried out following Gonçalves' protocol [92]. Briefly, circular coverslips measuring 0.130 mm in diameter were placed in a 24-well plate, and 30×10^3 cells per well were cultivated. After 2 h of cell adhesion, the control (same water volume) and V_{15} (4.30 and 8.60 µM) were added. After 24 h, the cells were washed with 0.100 M sodium cacodylate and fixed with 2.5% glutaraldehyde in 0.100 M sodium cacodylate buffer at pH 7.20 and kept for 1 h at room temperature. Then, the coverslips were washed twice with 0.100 M sodium cacodylate with a 10 min interval between each wash and fixed with 1% osmium tetroxide in 0.100 M sodium cacodylate buffer at pH 7.2 for 30 min in the absence of light. They were washed again twice with 0.100 M sodium cacodylate with a 10 min interval between washes. In the dehydration step, the cells were washed with ethanol at different concentrations (from 50% up to 100%) with a 10-min interval between washes. After the critical point was performed, the samples were metallized with gold, and SEM images were obtained with the Electronic Scanning Microscope TESCAN ORSAY HOLDING MIRA3 (Brno, Czech Republic).

3.9. Gene Expression Quantification

The MDA-MB-231 cells (8×10^5) were plated in P100 culture plates in quintuplicate and treated for 48 h with V_{15} at the obtained IC_{50} concentration. The total RNA was extracted using the AllPrep DNA/RNA Mini Kit (Qiagen, Hilden, Germany), and Reverse transcription was performed with SuperScript IV Reverse Transcription Kits (Invitrogen, Waltham, MA, USA) according to the manufacturer's instructions. Quantitative PCR experiments were performed using SYBR Green Power Master Mix, following the manufacturer's protocols in the Step One Plus equipment (Applied Biosystems, Foster City, CA, USA). The reference transcript used for gene normalization was *GAPDH*. In terms of efficiency, we used the pattern curve for each primer, and the acceptable value was more than 98% efficiency. The obtained results were analyzed using the_Ct method and further processed using the $2^{-\Delta\Delta Ct}$ [93]. The primer sequences are listed in Table S1.

4. Conclusions

In the present study, a mixed-valence polyoxovanadate, $[ClV^{V}_{7}V^{IV}_{8}O_{36}]$ (V_{15}), was studied against the MDA-MB-231 cancer cell line and analyzed its Ca^{2+}-ATPase inhibition potential. Moreover, the electrostatic potential map of V_{15}, V_{10}, $PV_{14\,ox}$, MnV_{13}, and Nb_{10} was correlated with the Ca^{2+}-ATPase activity inhibition. We believed that this kind of interdisciplinary collaborations, although not always easy to be achieved, are needed and represents a key cog in the "clock of the knowledge", dynamically joining several scientific wheels such as chemistry, biology, and medicine, among others, for achieving perfect shared innovation and development [94], particularly for the understanding of the effects of POMs in biological systems and their putative applications in medicine.

Thus, we first analyzed the V_{15} inhibitory potential for Ca^{2+}-ATPase activity using a coupled enzymatic method. It was determined that V_{15} presented an IC_{50} value of 14.2 µM and a mixed type of inhibition (Figure 10a). By affecting a key protein involved in cellular Ca^{2+} homeostasis, V_{15} might interfere with several physiological and pathological processes. ^{51}V-NMR and UV/Vis studies of V_{15} indicated its stability in the enzymatic and RPMI media used. In fact, V_{15} also exhibited cytotoxicity against MDA-MB-231 (IC_{50} = 17.2 µM) and MCF-7 (IC_{50} = 15.1 µM) breast cancer cells, determined after 24 h (Figure 10b). Furthermore, using V_{15} concentrations equivalent to half and 1/4 of the IC_{50}, MDA-MB321 cell migration was prevented by 70% and 90%, after 24 h, respectively (Figure 10c). Also, the fusiform morphology characteristic of the MDA-MB-231 cell line was lost to an epithelial-like (amoeboid) morphology upon exposure to V_{15}, which is a

potential advantage to control the tumor growth and progression (Figure 10d). Finally, it was observed that V_{15} induces an increase in the expression of the genes *RIPK1*, *MLKL*, and *RIPK3*, up to 3, 10, and 15-fold, respectively, pointing out that the mechanisms of cell death caused by V_{15} in the triple-negative breast cancer cell line may occur by necroptosis (Figure 10e). Putting it all together, V_{15}, which targets Ca^{2+}-ATPase with high affinity, has shown promising anticancer activities against breast cancer cells, and is worthy of being explored for therapeutic applications as well as for other areas of research.

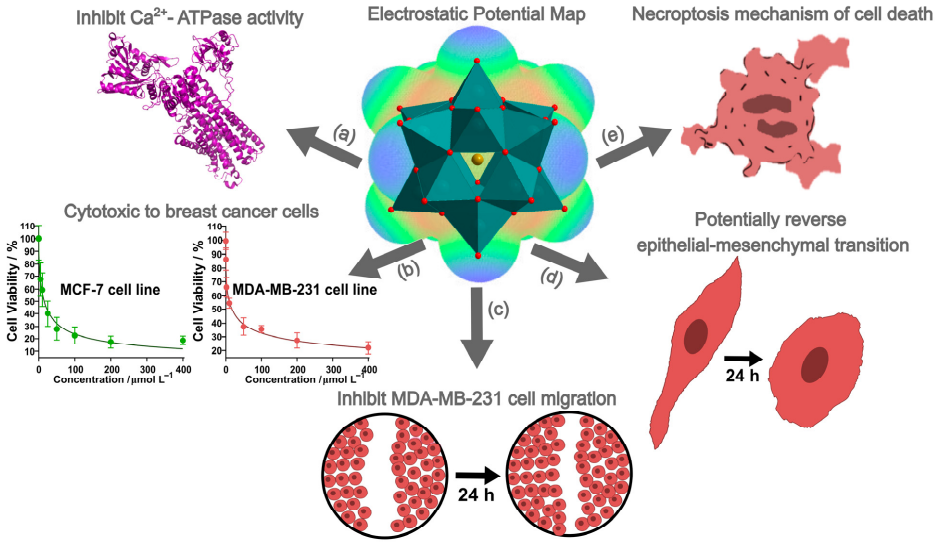

Figure 10. Compilation of the results obtained for V_{15} in this work: (**a**) Inhibition of Ca^{2+}-ATPase activity; (**b**) Cytotoxicity to breast cancer cell lines MCF-7 and MDA-MB-231; (**c**) Inhibition of MDA-MB-231 cell migration; (**d**) Potentially reverse epithelial–mesenchymal transition, and (**e**) Showed necroptosis mechanism of cell death.

Supplementary Materials: The following supporting information can be downloaded at: https://www.mdpi.com/article/10.3390/inorganics13090306/s1, Table S1: Primers sequence used for gene expression quantification in Homo sapiens; Figure S1: EPR spectra recorded at 77 K for V_{15} at 1.00 mM. (a) in aqueous solution, (b) in an enzymatic medium HEPES, and (c) in RPMI cell medium. Figure S2: Calibration curve constructed by plotting absorbance measured at λ = 950 nm vs. concentration of V_{15} in aqueous solution; Figure S3: Effects of V_{15} on cell viability using the MTT assay. In (a), the concentration curve and (b) IC_{50} curve fit for MCF-7 cells. In (c) concentration curve and (d) IC_{50} curve fit for MDA-MB-231 cells; Figure S4: Time curve of V_{15} in incubation times of 24, 48, and 72 h. In (a) to MCF-7 cells and in (b) to MDA-MB-231 cells. OD (Optic Density) was measured at 540 nm. **** means $p < 0.001$; Figure S5: Scanning Electron Microscopy (SEM) images for V_{15} in MDA-MB-231 cell line, at magnifications of 1000×, 2500×, 5000×, and 10,000× for (a) control; (b) concentration of 0.500 μmol L^{-1} and (c) 1.00 μmol L^{-1}. Figure S6: Infrared spectra of V_{15} recorded in KBr pellets for: (a) freshly synthesized sample, (b) after two months of aging, and (c) after two years of aging. Figure S7: Powder X-ray diffraction patterns of V_{15}, comparing the experimental with the simulated diffractogram generated from the single-crystal X-ray diffraction data CIF file number 794586.

Author Contributions: Conceptualization, M.A., G.G.N. and G.K.; methodology and formal analysis, M.A., G.K., G.F., E.L.d.S., R.R.R. and C.C.d.O.; investigation, G.F., B.R.B., H.d.S.C. and A.F.d.C.; writing—review and editing, G.F., M.A., G.G.N., G.K., B.R.B. and H.d.S.C.; funding acquisition, M.A., G.G.N. and G.K. All authors have read and agreed to the published version of the manuscript.

Funding: This research was funded by Portuguese national funds from FCT—Foundation for Science and Technology. This study was academically funded by government agencies with no private resources. Technology, grant number project UIDB/04326/2020, UIDP/04326/2020 and

LA/P/0101/2020, and by the Conselho Nacional de Desenvolvimento Científico e Tecnológico (CNPq, Project No. 310107/2025-3 and 403533/2025-2) and pesquisa/PRPPG/UFPR (04/2023).

Data Availability Statement: The original contributions presented in the study are included in the article/Supplementary Material, further inquiries can be directed to the corresponding authors.

Acknowledgments: M.A. gives thanks to Algarve University and the Portuguese national funds from FCT—Foundation for Science and Technology through project UIDB/04326/2020 (DOI:10.54499/UIDB/04326/2020), UIDP/04326/2020 (DOI:10.54499/UIDP/04326/2020), and LA/P/0101/2020 (DOI:10.54499/LA/P/0101/2020). E.L.d.S., H.d.S.C., and G.G.N. are grateful to the Centro Nacional de Processamento de Alto Desempenho (CENAPAD-SP) for providing access to computational infrastructure. The authors thank *Centro de Microscopia Eletrônica (CME-UFPR)* for the SEM analysis. B. R. B. and H.d.S.C. thank Coordenação de Aperfeiçoamento de Pessoal de Nível Superior (CAPES-PROEX and CAPES-PrInt, Finance Code 001), A.F.d.C. thanks CNPq for research grants and scholarships, G.G.N. thanks to Conselho Nacional de Desenvolvimento Científico e Tecnológico (CNPq grant 310107/2025-3 and 403533/2025-2)

Conflicts of Interest: The authors declare no conflicts of interest.

Abbreviations

The following abbreviations are used in this manuscript:

MCF-7	Michigan Cancer Foundantion-7
MDA-MB-231	Monroe Dunaway Anderson Cancer Center-Mammary/Breast-231
FBS	Fetal Bovine Serum
RPMI	Roswell Park Memorial Institute
DMEM	Dulbecco's Modified Eagle's Medium
HEPES	4-(2-hidroxyethyl)1-piperazine ethane sulfonic acid
PBS	Phosphate-Buffered Saline
PIPE	Piperazine-n,n'-Bis(2-ethanesulphonicAcid)
MTT	3-(4,5-dimethyltiazol-2-yl)-2,5-diphenyl-tetrazolium bromide
POMs	Polyoxometalates
POVs	Polyoxovanadates
MV-POVs	Mixed-Valence Polyoxovanadates
acac	Acetylacetonate
5-Fu	5-Fluorouracyl
ROS	Reactive Oxygen Species
^{51}V-NMR	Nuclear Magnetic Resonance of Vanadium 51
UV-Vis/NIR	Ultraviolet-Visible/Near-Infrared spectroscopy
SEM	Scanning Electron Microscopy
ESP	Electrostatic Surface Potential
LHR	Luteinizing Hormone Receptor
ATP	Adenosine Triphosphate
ABC	ATP-Binding Cassette
CHO	Chinese Hamster Ovary
P-gp	P-glycoprotein
EMT	Epithelial–Mesenchymal Transition
HER2	Human Epidermal Growth Factor Receptor 2
RIPK1	Receptor-Interacting Serine/Threonine-Protein Kinase 1
RIPK2	Receptor-Interacting Serine/Threonine-Protein Kinase 2
RIPK3	Receptor-Interacting Serine/Threonine-Protein Kinase 3
BAX	Bcl-2-Associated X Protein;
BCL2	B-Cell Lymphoma 2
TP53	Tumor Protein p53
CASP8	Caspase-8
MLKL	Mixed Lineage Kinase Domain-Like Protein

GAPDH	Glyceraldehyde-3-Phosphate Dehydrogenase
SR	Sarcoplasmic Reticulum
SERCA	Sarcoplasmic/Endoplasmic Reticulum Calcium ATPase
IC_{50}	Half Maximal Inhibitory Concentration
LB	Luria–Bertani
TNG	Triple-Negative
ER	Estrogen Receptor
PR	Progesterone Receptor

References

1. Aureliano, M. Decavanadate: A Journey in a Search of a Role. *Dalton Trans.* **2009**, *42*, 9093–9100. [CrossRef]
2. De Sousa-Coelho, A.L.; Aureliano, M.; Fraqueza, G.; Serrão, G.; Gonçalves, J.; Sánchez-Lombardo, I.; Link, W.; Ferreira, B.I. Decavanadate and Metformin-Decavanadate Effects in Human Melanoma Cells. *J. Inorg. Biochem.* **2022**, *235*, 111915. [CrossRef]
3. Soman, S.K.; Woodruff, M.R.J.; Dagda, R.K. The Mitochondrial Foundations of Parkinson's Disease: Therapeutic Implications. *Aging Dis.* **2025**, *16*, 2695–2720. [CrossRef]
4. Rathi, K.; Bhole, R.; Bansode, P.; Motghare, N. Navigating the Landscape of Alzheimer's Disease: From Epidemiology to Drug Re-Purposing. *Adv. Pharmacol. Pharm.* **2024**, *12*, 135–148. [CrossRef]
5. Hu, H.; Liang, W.; Ding, G. Ion Homeostasis in Diabetic Kidney Disease. *Trends Endocrinol. Metab.* **2024**, *35*, 142–150. [CrossRef] [PubMed]
6. Zaichick, S.V.; McGrath, K.M.; Caraveo, G. The Role of Ca^{2+} Signaling in Parkinson's Disease. *Dis. Model Mech.* **2017**, *10*, 519–535. [CrossRef]
7. Dowling, P.; Swandulla, D.; Ohlendieck, K. Biochemical and Proteomic Insights into Sarcoplasmic Reticulum Ca^{2+}-ATPase Complexes in Skeletal Muscles. *Expert Rev. Proteom.* **2023**, *20*, 125–142. [CrossRef] [PubMed]
8. Aureliano, M.; Fraqueza, G.; Ohlin, C.A. Ion Pumps as Biological Targets for Decavanadate. *Dalton Trans.* **2013**, *42*, 11770–11777. [CrossRef]
9. Sukumaran, P.; Nascimento Da Conceicao, V.; Sun, Y.; Ahamad, N.; Saraiva, L.R.; Selvaraj, S.; Singh, B.B. Calcium Signaling Regulates Autophagy and Apoptosis. *Cells* **2021**, *10*, 2125. [CrossRef] [PubMed]
10. Bijelic, A.; Aureliano, M.; Rompel, A. Polyoxometalates as Potential Next-Generation Metallodrugs in the Combat Against Cancer. *Angew. Chem. Int. Ed.* **2019**, *58*, 2980–2999. [CrossRef]
11. Kumari, N.; Pullaguri, N.; Rath, S.N.; Bajaj, A.; Sahu, V.; Ealla, K.K.R. Dysregulation of Calcium Homeostasis in Cancer and Its Role in Chemoresistance. *Cancer Drug Resist.* **2024**, *7*, 11. [CrossRef]
12. Fraqueza, G.; Fuentes, J.; Krivosudský, L.; Dutta, S.; Mal, S.S.; Roller, A.; Giester, G.; Rompel, A.; Aureliano, M. Inhibition of Na+/K+-and Ca^{2+}-ATPase Activities by Phosphotetradecavanadate. *J. Inorg. Biochem.* **2019**, *197*, 110700. [CrossRef]
13. Poejo, J.; Gumerova, N.I.; Rompel, A.; Mata, A.M.; Aureliano, M.; Gutierrez-Merino, C. Unveiling the Agonistic Properties of Preyssler-Type Polyoxotungstates on Purinergic P2 Receptors. *J. Inorg. Biochem.* **2024**, *259*, 112640. [CrossRef]
14. Ferraro, G.; Garribba, E.; Merlino, A. Exploring Polyoxidovanadate–Protein Interaction. *Trends Chem.* **2025**, *7*, 3–6. [CrossRef]
15. Aronica, C.; Chastanet, G.; Zueva, E.; Borshch, S.A.; Clemente-Juan, J.M.; Luneau, D. A Mixed-Valence Polyoxovanadate(III, IV) Cluster with a Calixarene Cap Exhibiting Ferromagnetic V(III)−V(IV) Interactions. *J. Am. Chem. Soc.* **2008**, *130*, 2365–2371. [CrossRef]
16. Solé-Daura, A.; Notario-Estévez, A.; Carbó, J.J.; Poblet, J.M.; de Graaf, C.; Monakhov, K.Y.; López, X. How Does the Redox State of Polyoxovanadates Influence the Collective Behavior in Solution? A Case Study with $[I@V_{18}O_{42}]^{q-}$ (q = 3, 5, 7, 11, and 13). *Inorg. Chem.* **2019**, *58*, 3881–3894. [CrossRef] [PubMed]
17. Zhang, T.; Yan, W.; Wang, Y.; Wang, J.; Liu, C.; Ye, F.; Liu, B. An Ecofriendly and Efficient Wood-Based Polyoxovanadate Solar Evaporation Generator. *Sci. China Mater.* **2023**, *66*, 3292–3299. [CrossRef]
18. Aureliano, M.; Gumerova, N.I.; Sciortino, G.; Garribba, E.; Rompel, A.; Crans, D.C. Polyoxovanadates with Emerging Biomedical Activities. *Coord. Chem. Rev.* **2021**, *447*, 214143. [CrossRef]
19. Müller, A.; Krickemeyer, E.; Penk, M.; Walberg, H.; Bögge, H. Spherical Mixed-Valence $[V_{15}O_{36}]^{5-}$, an Example from an Unusual Cluster Family. *Angew. Chem. Int. Ed.* **1987**, *26*, 1045–1046. [CrossRef]
20. Postal, K.; Maluf, D.F.; Valdameri, G.; Rüdiger, A.L.; Hughes, D.L.; de Sá, E.L.; Ribeiro, R.R.; de Souza, E.M.; Soares, J.F.; Nunes, G.G. Chemoprotective Activity of Mixed Valence Polyoxovanadates against Diethylsulphate in E. Coli Cultures: Insights from Solution Speciation Studies. *RSC Adv.* **2016**, *6*, 114955–114968. [CrossRef]
21. Kita, D.H.; Andrade, G.A.; Missina, J.M.; Postal, K.; Boell, V.K.; Santana, F.S.; Zattoni, I.F.; Zanzarini, I.D.S.; Moure, V.R.; Rego, F.G.D.M.; et al. Polyoxovanadates as New P-glycoprotein Inhibitors: Insights into the Mechanism of Inhibition. *FEBS Lett.* **2022**, *596*, 381–399. [CrossRef] [PubMed]

22. Althumairy, D.; Postal, K.; Barisas, B.G.; Nunes, G.G.; Roess, D.A.; Crans, D.C. Polyoxometalates Function as Indirect Activators of a G Protein-Coupled Receptor. *Metallomics* **2020**, *12*, 1044–1061. [CrossRef]
23. Tito, G.; Ferraro, G.; Garribba, E.; Merlino, A. Formation of Mixed-Valence Cage-Like Polyoxidovanadates at 37 °C Upon Reaction of $V^{IV}O$(Acetylacetonato)$_2$ with Lysozyme. *Chem. A Eur. J.* **2025**, *31*, e202500488. [CrossRef]
24. Lucignano, R.; Tito, G.; Ferraro, G.; Picone, D.; Pisanu, F.; Garribba, E.; Merlino, A. Spherical Mixed-Valence Pentadecavanadate Binding to Human H-Chain Ferritin. *Inorg. Chem. Front.* **2025**. [CrossRef]
25. Essid, A.; Elbini, I.; Ksiksi, R.; Harrab, N.; Moslah, W.; Jendoubi, I.; Doghri, R.; Zid, M.-F.; Luis, J.; Srairi-Abid, N. Decavanadate Compound Displays In Vitro and In Vivo Antitumor Effect on Melanoma Models. *Bioinorg. Chem. Appl.* **2025**, *2025*, 6680022. [CrossRef]
26. Yao, C.; Zhao, Z.; Tan, T.; Yan, J.; Chen, Z.; Xiong, J.; Li, H.; Wei, Y.; Hu, K. Lindqvist-Type Polyoxometalates Act as Anti-Breast Cancer Drugs via Mitophagy-Induced Apoptosis. *Curr. Med. Sci.* **2024**, *44*, 809–819. [CrossRef]
27. Soares, S.S.; Martins, H.; Duarte, R.O.; Moura, J.J.G.; Coucelo, J.; Gutiérrez-Merino, C.; Aureliano, M. Vanadium Distribution, Lipid Peroxidation and Oxidative Stress Markers upon Decavanadate in Vivo Administration. *J. Inorg. Biochem.* **2007**, *101*, 80–88. [CrossRef]
28. Barbosa, M.D.M.; de Lima, L.M.A.; Alves, W.A.D.S.; de Lima, E.K.B.; da Silva, L.A.; da Silva, T.D.; Postal, K.; Ramadan, M.; Kostenkova, K.; Gomes, D.A.; et al. In Vitro, Oral Acute, and Repeated 28-Day Oral Dose Toxicity of a Mixed-Valence Polyoxovanadate Cluster. *Pharmaceuticals* **2023**, *16*, 1232. [CrossRef]
29. Nunes, G.G.; Bonatto, A.C.; de Albuquerque, C.G.; Barison, A.; Ribeiro, R.R.; Back, D.F.; Andrade, A.V.C.; de Sá, E.L.; Pedrosa, F.D.O.; Soares, J.F.; et al. Synthesis, Characterization and Chemoprotective Activity of Polyoxovanadates against DNA Alkylation. *J. Inorg. Biochem.* **2012**, *108*, 36–46. [CrossRef] [PubMed]
30. Bray, F.; Laversanne, M.; Sung, H.; Ferlay, J.; Siegel, R.L.; Soerjomataram, I.; Jemal, A. Global Cancer Statistics 2022: GLOBOCAN Estimates of Incidence and Mortality Worldwide for 36 Cancers in 185 Countries. *CA Cancer J. Clin.* **2024**, *74*, 229–263. [CrossRef] [PubMed]
31. Orrantia-Borunda, E.; Anchondo-Nuñez, P.; Acuña-Aguilar, L.E.; Gómez-Valles, F.O.; Ramírez-Valdespino, C.A. Subtypes of Breast Cancer. In *Breast Cancer*; Exon Publications: Brisbane, Australia, 2022; pp. 31–42.
32. Bonotto, M.; Gerratana, L.; Poletto, E.; Driol, P.; Giangreco, M.; Russo, S.; Minisini, A.M.; Andreetta, C.; Mansutti, M.; Pisa, F.E.; et al. Measures of Outcome in Metastatic Breast Cancer: Insights From a Real-World Scenario. *Oncologist* **2014**, *19*, 608–615. [CrossRef]
33. Schirrmacher, V. From Chemotherapy to Biological Therapy: A Review of Novel Concepts to Reduce the Side Effects of Systemic Cancer Treatment (Review). *Int. J. Oncol.* **2018**, *54*, 407–419. [CrossRef]
34. Wang, J.; Wu, S.-G. Breast Cancer: An Overview of Current Therapeutic Strategies, Challenge, and Perspectives. *Breast Cancer Targets Ther.* **2023**, *15*, 721–730. [CrossRef]
35. Lee, J.S.; Yost, S.E.; Yuan, Y. Neoadjuvant Treatment for Triple Negative Breast Cancer: Recent Progresses and Challenges. *Cancers* **2020**, *12*, 1404. [CrossRef] [PubMed]
36. Shen, G.; Liu, Z.; Wang, M.; Zhao, Y.; Liu, X.; Hou, Y.; Ma, W.; Han, J.; Zhou, X.; Ren, D.; et al. Neoadjuvant Apatinib Addition to Sintilimab and Carboplatin-Taxane Based Chemotherapy in Patients with Early Triple-Negative Breast Cancer: The Phase 2 NeoSAC Trial. *Signal Transduct. Target. Ther.* **2025**, *10*, 41. [CrossRef]
37. Bishayee, A.; Waghray, A.; Patel, M.A.; Chatterjee, M. Vanadium in the Detection, Prevention and Treatment of Cancer: The in Vivo Evidence. *Cancer Lett.* **2010**, *294*, 1–12. [CrossRef] [PubMed]
38. Aureliano, M.; Camilo, H.S.; Brito, B.R.; Ribeiro, R.R.; Fraqueza, G.; Klassen, G.; Nunes, G.G. Polyoxovanadates with Anti-breastCancer Activity and Ca^{2+}-ATPase Inhibition Potential. *Eur. Assoc. Cancer Res.* **2025**, *19*, 511–512. [CrossRef]
39. Wang, C.; Dai, Z.; Zhang, Q.; Li, X.; Ma, M.; Shi, Z.; Zhang, J.; Liu, Q.; Chen, H. A Bifunctional Biomineralized Polyoxometalate Enabling Efficient Non-Inflammatory NIR-II Photothermal Tumor Therapy. *Chem. Eng. J.* **2024**, *490*, 151601. [CrossRef]
40. Misra, A.; Kozma, K.; Streb, C.; Nyman, M. Beyond Charge Balance: Counter-Cations in Polyoxometalate Chemistry. *Angew. Chem. Int. Ed.* **2020**, *59*, 596–612. [CrossRef]
41. Gumerova, N.I.; Rompel, A. Speciation Atlas of Polyoxometalates in Aqueous Solutions. *Sci. Adv.* **2023**, *9*, eadi0814. [CrossRef]
42. Tito, G.; Ferraro, G.; Pisanu, F.; Garribba, E.; Merlino, A. Non-Covalent and Covalent Binding of New Mixed-Valence Cage-like Polyoxidovanadate Clusters to Lysozyme. *Angew. Chem. Int. Ed.* **2024**, *63*, e202406669. [CrossRef] [PubMed]
43. Gumerova, N.I.; Rompel, A. Polyoxometalates in Solution: Speciation under Spotlight. *Chem. Soc. Rev.* **2020**, *49*, 7568–7601. [CrossRef]
44. Day, P.; Hush, N.S.; Clark, R.J.H. Mixed Valence: Origins and Developments. *Philos. Trans. R. Soc. A Math. Phys. Eng. Sci.* **2008**, *366*, 5–14. [CrossRef]
45. Aureliano, M. Recent Perspectives into Biochemistry of Decavanadate. *World J. Biol. Chem.* **2011**, *2*, 215–225. [CrossRef]
46. Fraqueza, G.; Ohlin, C.A.; Casey, W.H.; Aureliano, M. Sarcoplasmic Reticulum Calcium ATPase Interactions with Decaniobate, Decavanadate, Vanadate, Tungstate and Molybdate. *J. Inorg. Biochem.* **2012**, *107*, 82–89. [CrossRef]

47. Marques-da-Silva, D.; Fraqueza, G.; Lagoa, R.; Vannathan, A.A.; Mal, S.S.; Aureliano, M. Polyoxovanadate Inhibition of *Escherichia Coli* Growth Shows a Reverse Correlation with Ca^{2+}-ATPase Inhibition. *New J. Chem.* **2019**, *43*, 17577–17587. [CrossRef]
48. Gumerova, N.; Krivosudský, L.; Fraqueza, G.; Breibeck, J.; Al-Sayed, E.; Tanuhadi, E.; Bijelic, A.; Fuentes, J.; Aureliano, M.; Rompel, A. The P-Type ATPase Inhibiting Potential of Polyoxotungstates. *Metallomics* **2018**, *10*, 287–295. [CrossRef]
49. Fraqueza, G.; Batista de Carvalho, L.A.E.; Marques, M.P.M.; Maia, L.; Ohlin, C.A.; Casey, W.H.; Aureliano, M. Decavanadate, Decaniobate, Tungstate and Molybdate Interactions with Sarcoplasmic Reticulum Ca^{2+}-ATPase: Quercetin Prevents Cysteine Oxidation by Vanadate but Does Not Reverse ATPase Inhibition. *Dalton Trans.* **2012**, *41*, 12749–12758. [CrossRef]
50. Aureliano, M.; Fraqueza, G.; Berrocal, M.; Cordoba-Granados, J.J.; Gumerova, N.I.; Rompel, A.; Gutierrez-Merino, C.; Mata, A.M. Inhibition of SERCA and PMCA Ca^{2+}-ATPase Activities by Polyoxotungstates. *J. Inorg. Biochem.* **2022**, *236*, 111952. [CrossRef]
51. Sciortino, G.; Aureliano, M.; Garribba, E. Rationalizing the Decavanadate(V) and Oxidovanadium(IV) Binding to G-Actin and the Competition with Decaniobate(V) and ATP. *Inorg. Chem.* **2021**, *60*, 334–344. [CrossRef] [PubMed]
52. Toyoshima, C.; Nakasako, M.; Nomura, H.; Ogawa, H. Crystal Structure of the Calcium Pump of Sarcoplasmic Reticulum at 2.6 Å Resolution. *Nature* **2000**, *405*, 647–655. [CrossRef] [PubMed]
53. Hua, S.; Inesi, G.; Toyoshima, C. Distinct Topologies of Mono- and Decavanadate Binding and Photo-Oxidative Cleavage in the Sarcoplasmic Reticulum ATPase. *J. Biol. Chem.* **2000**, *275*, 30546–30550. [CrossRef]
54. Aureliano, M.; Gumerova, N.I.; Sciortino, G.; Garribba, E.; McLauchlan, C.C.; Rompel, A.; Crans, D.C. Polyoxidovanadates' Interactions with Proteins: An Overview. *Coord. Chem. Rev.* **2022**, *454*, 214344. [CrossRef]
55. Zarroug, R.; Artetxe, B.; Ayed, B.; López, X.; Ribeiro, N.; Correia, I.; Pessoa, J.C. New Phosphotetradecavanadate Hybrids: Crystal Structure, DFT Analysis, Stability and Binding Interactions with Bio-Macromolecules. *Dalton Trans.* **2022**, *51*, 8303–8317. [CrossRef] [PubMed]
56. Solé-Daura, A.; Poblet, J.M.; Carbó, J.J. Structure–Activity Relationships for the Affinity of Chaotropic Polyoxometalate Anions towards Proteins. *Chem. A Eur. J.* **2020**, *26*, 5799–5809. [CrossRef] [PubMed]
57. Aybek, H.; Temel, Y.; Ahmed, B.M.; Ağca, C.A.; Çiftci, M. Deciphering of The Effect of Chemotherapeutic Agents on Human Glutathione S-Transferase Enzyme and MCF-7 Cell Line. *Protein Pept. Lett.* **2020**, *27*, 888–894. [CrossRef]
58. Hu, X.; Wang, H.; Huang, B.; Li, N.; Hu, K.; Wu, B.; Xiao, Z.; Wei, Y.; Wu, P. A New Scheme for Rational Design and Synthesis of Polyoxovanadate Hybrids with High Antitumor Activities. *J. Inorg. Biochem.* **2019**, *193*, 130–132. [CrossRef] [PubMed]
59. Kioseoglou, E.; Gabriel, C.; Petanidis, S.; Psycharis, V.; Raptopoulou, C.P.; Terzis, A.; Salifoglou, A. Binary Decavanadate-Betaine Composite Materials of Potential Anticarcinogenic Activity. *Z. Anorg. Allg. Chem.* **2013**, *639*, 1407–1416. [CrossRef]
60. Qi, W.; Zhang, B.; Qi, Y.; Guo, S.; Tian, R.; Sun, J.; Zhao, M. The Anti-Proliferation Activity and Mechanism of Action of $K_{12}[V_{18}O_{42}(H_2O)]\cdot 6H_2O$ on Breast Cancer Cell Lines. *Molecules* **2017**, *22*, 1535. [CrossRef]
61. Liu, H.; Zang, C.; Fenner, M.H.; Possinger, K.; Elstner, E. PPARγ Ligands and ATRA Inhibit the Invasion of Human Breast Cancer Cells in Vitro. *Breast Cancer Res. Treat.* **2003**, *79*, 63–74. [CrossRef]
62. Chavez, K.J.; Garimella, S.V.; Lipkowitz, S. Triple Negative Breast Cancer Cell Lines: One Tool in the Search for Better Treatment of Triple Negative Breast Cancer. *Breast Dis.* **2011**, *32*, 35–48. [CrossRef]
63. Ksiksi, R.; Essid, A.; Kouka, S.; Boujelbane, F.; Daoudi, M.; Srairi-Abid, N.; Zid, M.F. Synthesis and Characterization of a Tetra-(Benzylammonium) Dihydrogen Decavanadate Dihydrate Compound Inhibiting MDA-MB-231 Human Breast Cancer Cells Proliferation and Migration. *J. Mol. Struct.* **2022**, *1250*, 131929. [CrossRef]
64. Image, J. JS Software. Available online: https://Ij.Imjoy.Io/ (accessed on 16 June 2025).
65. Ghafoor, S.; Garcia, E.; Jay, D.J.; Persad, S. Molecular Mechanisms Regulating Epithelial Mesenchymal Transition (EMT) to Promote Cancer Progression. *Int. J. Mol. Sci.* **2025**, *26*, 4364. [CrossRef] [PubMed]
66. Kumar, V.; Abbas, A.K.; Aster, J.C. *Robbins & Cotran Patologia: Bases Patológicas Das Doenças*, 9th ed.; Elsevier: Rio de Janeiro, Brazil, 2016.
67. Liu, X.; Zhou, M.; Mei, L.; Ruan, J.; Hu, Q.; Peng, J.; Su, H.; Liao, H.; Liu, S.; Liu, W.; et al. Key Roles of Necroptotic Factors in Promoting Tumor Growth. *Oncotarget* **2016**, *7*, 22219–22233. [CrossRef]
68. Zheng, W.; Yang, L.; Liu, Y.; Qin, X.; Zhou, Y.; Zhou, Y.; Liu, J. Mo Polyoxometalate Nanoparticles Inhibit Tumor Growth and Vascular Endothelial Growth Factor Induced Angiogenesis. *Sci. Technol. Adv. Mater.* **2014**, *15*, 035010. [CrossRef] [PubMed]
69. Dianat, S.; Bordbar, A.K.; Tangestaninejad, S.; Zarkesh-Esfahani, S.H.; Habibi, P.; Abbasi Kajani, A. CtDNA Interaction of Co-Containing Keggin Polyoxomolybdate and in Vitro Antitumor Activity of Free and Its Nano-Encapsulated Derivatives. *J. Iran. Chem. Soc.* **2016**, *13*, 1895–1904. [CrossRef]
70. Dianat, S.; Bordbar, A.-K.; Tangestaninejad, S.; Yadollahi, B.; Amiri, R.; Zarkesh-Esfahani, S.-H.; Habibi, P. In Vitro Antitumor Activity of Free and Nano-Encapsulated $Na_5[PMo_{10}V_2O_{40}]\cdot nH_2O$ and Its Binding Properties with CtDNA by Using Combined Spectroscopic Methods. *J. Inorg. Biochem.* **2015**, *152*, 74–81. [CrossRef]
71. Dianat, S.; Bordbar, A.K.; Tangestaninejad, S.; Yadollahi, B.; Zarkesh-Esfahani, S.H.; Habibi, P. In Vitro Antitumor Activity of Parent and Nano-Encapsulated Mono Cobalt-Substituted Keggin Polyoxotungstate and Its CtDNA Binding Properties. *Chem. Biol. Interact.* **2014**, *215*, 25–32. [CrossRef] [PubMed]

72. Geisberger, G.; Gyenge, E.B.; Maake, C.; Patzke, G.R. Trimethyl and Carboxymethyl Chitosan Carriers for Bio-Active Polymer–Inorganic Nanocomposites. *Carbohydr. Polym.* **2013**, *91*, 58–67. [CrossRef]
73. Dianat, S.; Bordbar, A.K.; Tangestaninejad, S.; Yadollahi, B.; Zarkesh-Esfahani, S.H.; Habibi, P. CtDNA Binding Affinity and in Vitro Antitumor Activity of Three Keggin Type Polyoxotungestates. *J. Photochem. Photobiol. B Biol.* **2013**, *124*, 27–33. [CrossRef]
74. Yamase, T. Polyoxometalates for Molecular Devices: Antitumor Activity and Luminescence. *Mol. Eng.* **1994**, *3*, 241–262. [CrossRef]
75. Carvalho, F.; Aureliano, M. Polyoxometalates Impact as Anticancer Agents. *Int. J. Mol. Sci.* **2023**, *24*, 5043. [CrossRef] [PubMed]
76. Faizan, M.I.; Ahmad, T. Altered Mitochondrial Calcium Handling and Cell Death by Necroptosis: An Emerging Paradigm. *Mitochondrion* **2021**, *57*, 47–62. [CrossRef]
77. Ohlin, C.A.; Villa, E.M.; Fettinger, J.C.; Casey, W.H. A New Titanoniobate Ion—Completing the Series $[Nb_{10}O_{28}]^{6-}$, $[TiNb_9O_{28}]^{7-}$ and $[Ti_2Nb_8O_{28}]^{8-}$. *Dalton Trans.* **2009**, *15*, 2677–2678. [CrossRef]
78. Li, D.; Liu, S.; Sun, C.; Xie, L.; Wang, E.; Hu, N.; Jia, H. A Novel 2D Layered Network Based on 13-Vanadomanganate(IV): $K_3(HABOB)_4[MnV_{13}O_{38}]\cdot 9H_2O$ (ABOB=N-Amidino-4-Morpholincarboxamidine). *Inorg. Chem. Commun.* **2005**, *8*, 433–436. [CrossRef]
79. Missina, J.M.; Gavinho, B.; Postal, K.; Santana, F.S.; Valdameri, G.; de Souza, E.M.; Hughes, D.L.; Ramirez, M.I.; Soares, J.F.; Nunes, G.G. Effects of Decavanadate Salts with Organic and Inorganic Cations on *Escherichia coli*, *Giardia intestinalis*, and Vero Cells. *Inorg. Chem.* **2018**, *57*, 11930–11941. [CrossRef]
80. Grimme, S.; Ehrlich, S.; Goerigk, L. Effect of the Damping Function in Dispersion Corrected Density Functional Theory. *J Comput. Chem.* **2011**, *32*, 1456–1465. [CrossRef]
81. Chai, J.-D.; Head-Gordon, M. Long-Range Corrected Hybrid Density Functionals with Damped Atom–Atom Dispersion Corrections. *Phys. Chem. Chem. Phys.* **2008**, *10*, 6615–6620. [CrossRef]
82. Weigend, F.; Ahlrichs, R. Balanced Basis Sets of Split Valence, Triple Zeta Valence and Quadruple Zeta Valence Quality for H to Rn: Design and Assessment of Accuracy. *Phys. Chem. Chem. Phys.* **2005**, *7*, 3297–3305. [CrossRef]
83. Neese, F. Software Update: The ORCA Program System—Version 5.0. *WIREs Comput. Mol. Sci.* **2022**, *12*, e1606. [CrossRef]
84. Lu, T.; Chen, F. Multiwfn: A Multifunctional Wavefunction Analyzer. *J. Comput. Chem.* **2012**, *33*, 580–592. [CrossRef]
85. Lu, T.; Chen, F. Quantitative Analysis of Molecular Surface Based on Improved Marching Tetrahedra Algorithm. *J. Mol. Graph. Model.* **2012**, *38*, 314–323. [CrossRef] [PubMed]
86. Lu, T. A Comprehensive Electron Wavefunction Analysis Toolbox for Chemists, Multiwfn. *J. Chem. Phys.* **2024**, *161*, 082503. [CrossRef]
87. Humphrey, W.; Dalke, A.; Schulten, K. VMD: Visual Molecular Dynamics. *J. Mol. Graph.* **1996**, *14*, 33–38. [CrossRef]
88. Pantazis, D.A.; Chen, X.-Y.; Landis, C.R.; Neese, F. All-Electron Scalar Relativistic Basis Sets for Third-Row Transition Metal Atoms. *J. Chem. Theory Comput.* **2008**, *4*, 908–919. [CrossRef]
89. Van de Loosdrecht, A.A.; Beelen, R.H.J.; Ossenkoppele, G.J.; Broekhoven, M.G.; Langenhuijsen, M.M.A.C. A Tetrazolium-Based Colorimetric MTT Assay to Quantitate Human Monocyte Mediated Cytotoxicity against Leukemic Cells from Cell Lines and Patients with Acute Myeloid Leukemia. *J. Immunol. Methods* **1994**, *174*, 311–320. [CrossRef]
90. GraphPad Software, Inc. *GraphPad Prism—Version 7.0 for Windows*; GraphPad Prism: Boston, MA, USA, 2018.
91. Serio, F.; da Cruz, A.F.; Chandra, A.; Nobile, C.; Rossi, G.R.; D'Amone, E.; Gigli, G.; del Mercato, L.L.; de Oliveira, C.C. Electrospun Polyvinyl-Alcohol/Gum Arabic Nanofibers: Biomimetic Platform for in Vitro Cell Growth and Cancer Nanomedicine Delivery. *Int. J. Biol. Macromol.* **2021**, *188*, 764–773. [CrossRef]
92. Gonçalves, J.P.; de Oliveira, C.C.; da Silva Trindade, E.; Riegel-Vidotti, I.C.; Vidotti, M.; Simas, F.F. In Vitro Biocompatibility Screening of a Colloidal Gum Arabic-Polyaniline Conducting Nanocomposite. *Int. J. Biol. Macromol.* **2021**, *173*, 109–117. [CrossRef] [PubMed]
93. Livak, K.J.; Schmittgen, T.D. Analysis of Relative Gene Expression Data Using Real-Time Quantitative PCR and the $2^{-\Delta\Delta CT}$ Method. *Methods* **2001**, *25*, 402–408. [CrossRef]
94. Aureliano, M.; Ma, B. Feature Papers in BioChem. *BioChem* **2025**, *5*, 17. [CrossRef]